Effect of High-Pressure Torsion and Natural Ageing on Hardness, Electrical Resistivity and Fatigue Properties of Commercially Pure Cu

A Thesis

submitted towards the fulfilment of

the requirements for the degree of

M.Tech. (Research)

in

Materials Engineering

by

Ajay Rijal

Under the Guidance of

Dr. Praveen Kumar

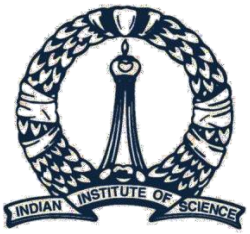

Department of Materials Engineering

Indian Institute of Science, Bangalore

January 2020

ACKNOWLEDGEMENTS

I would like to thank Dr. Praveen Kumar for his guidance, motivation, and support throughout the journey at IISc. Without his guidance this dissertation would not have been possible.

I would like to thank Professor Megumi Kawasaki and her PhD student Mr. J. K. Han of Oregon State University, USA for providing HPT Cu samples.

I would like to thank Dr. Thomas Straub, Dr. Tobias Kennerknecht and Professor Christoph Eberl of Fraunhofer Institute for Mechanics of Materials (IWM) Freiburg, Germany for help with conducting fatigue tests.

I would like to thank Professor Chandan Srivastava and Dr. Rekha M Y for help with TEM sample preparation. I would also like to thank Dr. Abhishek Sharma, Mahender, Ujjawal and Manu for help with TEM sample preparation and analysis.

I am grateful to Professor Indradev Samajdar of IIT Bombay, Mumbai for conducting EBSD of the few samples.

I would like to thank Mr. Shobhit Pratap Singh for help and guidance throughout my project and all my lab-mates (Dipali, Ali, Anwesha, Ananya, Swanand, Aditya, Chandan, Devi Lal, Faizan, Sachin, Raj, Vijayendra, Sumit and Priya) for their suggestions and healthy discussions.

I would like to thank my parents for their support and motivation.

(Ajay Rijal)

LIST OF PUBLICATIONS FROM THE WORK

1. Rijal, Ajay, Shobhit P. Singh, Jae-Kyung Han, Megumi Kawasaki, and Praveen Kumar. "Effect of High-Pressure Torsion on Hardness and Electrical Resistivity of Commercially Pure Cu." *Advanced Engineering Materials* 22, no. 1 (2020): 1900547.
2. Rijal, Ajay, Shobhit Pratap Singh, Jae-Kyung Han, Megumi Kawasaki, and Praveen Kumar. "Effect of HPT processing followed by long term natural ageing on mechanical and electrical properties of commercially pure Cu." *Lett. Mater.* 9, no. 4 (2019): 561-565.

TABLE OF CONTENTS

LISTS OF FIGURES

ABSTRACT

Commercially pure Cu was processed through high-pressure torsion (HPT) at a pressure of 6 GPa starting from ¼ up to 50 turns. These samples were then naturally aged for 1.75 years under the laboratory condition. Subsequently, microhardness, electrical resistivity, and fatigue response of samples in bending were evaluated and correlated with microstructure. Grain size monotonically decreased with the number of HPT turns and became saturated at ~300 nm after an equivalent strain of ~40. Low-angle grain boundaries and sub-grains were formed at the onset of straining, which transformed into high angle grain boundaries upon further straining. Hardness of the freshly processed samples monotonically increased with the HPT strain and saturated at the value of 155 HV; however, the samples processed to a shear strain of 2 to 20 and naturally aged for 1.75 years demonstrated a remarkable drop in the hardness values. Interestingly, the natural ageing was not effective in changing the hardness of HPT processed samples strained up to very high shear strains. Electrical resistivity of the HPT processed samples after natural ageing as well as freshly prepared samples showed a non-monotonous variation with the HPT strain, wherein it increased and then decreased and finally again started to increase with increasing shear strain. Maximum increment in the resistivity was about ~27% as compared to an annealed Cu sample, whereas microhardness enhanced by ~ 240 %. On other hand, during fatigue testing, the area fraction of surface cracks increased monotonically with the stress in both annealed and HPT processed samples. Furthermore, HPT processed Cu samples showed lesser fraction of surface cracks at low stresses, which indicates that HPT process assisted suppression of the surface crack formation and growth of cracks during the initial stages. In all segments of the work, an overview of the observed properties, based on correlation with microstructure conducted using electron back-scattered diffraction and transmission electron microscopy, is provided.

1. Introduction

Severe plastic deformation (SPD) is one of the major topics of interest in research due to its ability to produce ultrafine grains in metallic materials with an excellent combination of mechanical properties [1-4]. In a SPD processes, the bulk material is processed through the mechanical processing route through which a tremendous increment in the physical properties, such as like strength, creep resistance, fractures strength, etc., is achieved through the nano-structuring of material [5].

High-pressure torsion (HPT), accumulative rolling bonding (ARB) and equal channel angular pressing (ECAP) are some of the commonly used SPD processes. Schematics of these different SPD processes are shown in **Figure 1**. The major idea behind all the SPD processes is to impart a huge amount of strain into the samples to change its microstructure drastically. SPD processes produce a nano-structured material, wherein sub-grains are progressively converted into grains with high angle grain boundaries with strain [2-4]. The nanostructured material contains the grain with high energies, often referred as non-equilibrium boundaries. These materials are also called as ultra-fine grained (UFG) materials [6]. Among all the SPD processes, equal-channel angular pressing (ECAP), wherein a billet is pushed through a die with an angular channel bent at an angle of 90^{o} [7], and high-pressure torsion (HPT), which enables imposing severe torsional strains into a disk-shaped sample by placing it in between two anvils and rotating one of the anvils while applying a very large uniaxial compressive stress, [8] are the most extensively used techniques, primarily due to the ease of processing and their effectiveness in imposing very large strains into samples without cracking or fracture.

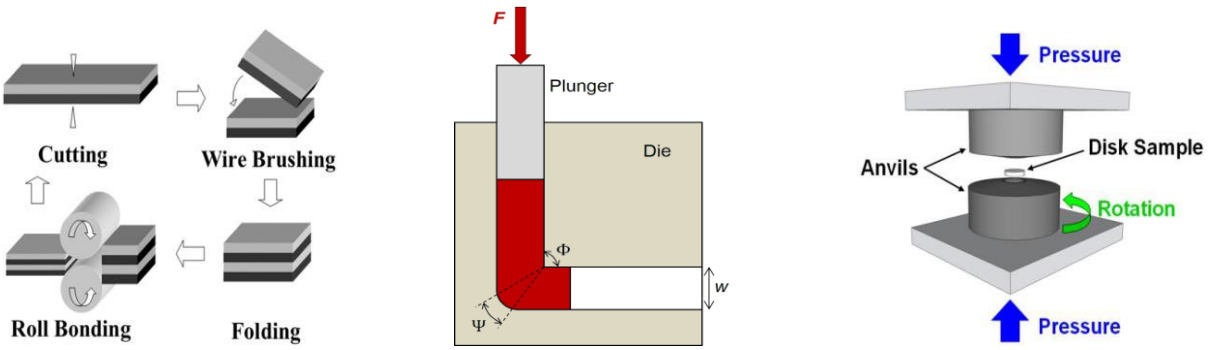

(a) (b) (c)

Figure 1: Schematics of different severe plastic deformation processes: (a) ARB [9], (b) ECAP [10] and (c) HPT [11]

In comparison to other SPD processes, HPT process is able to impose very high amount of strain producing the nano-scale grains having high fraction of high angle boundaries in a shorter processing time [12]. Such an ability of HPT makes it suitable for quickly studying the effect of extreme strains on structure-property relationship relevant for an application. The strain applied on the sample gradually varies with the distance from the center to the periphery as shown by the equation below [13],

$$\varepsilon_{ev} = \frac{2}{\sqrt{3}} \frac{\pi r N}{h} \quad (1)$$

where ε_{ev} is the equivalent von Mises strain at a point at r as indicated on the **Figure 2**, N is the number of turns, and h is the thickness of the sample (even, at the center region where strain is supposed to be zero as per the above equation, it has some shear strain due to misalignment of the anvils). Hence, HPT processing allows studying the effect of large plastic strain on the microstructure as well as the physical properties, through local probing, using only one sample. This could help in performing high throughput experiments and material combinatorics. Hence, studying the effects of gradient straining on multiple properties of a material processed by HPT is quite attractive and it is evident from the increasing popularity of HPT in the last two decades. Herein, the microstructure and various mechanical properties, such as hardness [14, 15], wear [16-19], etc., of various metals and alloys processed through HPT have been well studied. However, only a few reports have discussed the effect of HPT processing on electrical conductivity (or resistivity) of materials [20-24].

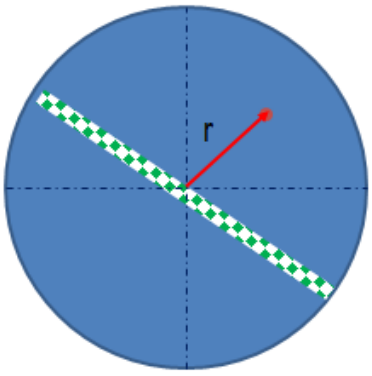

Figure 2. A schematic illustration of the sample, which also shows the radial coordinate. The shaded region shows a narrow strip along a diameter of the sample, along which hardness, resistivity, etc. can be measured as function of strain imposed by HPT.

Cu is an interesting metal for exploring techniques suitable for meeting the aforementioned challenge, as it is one of the most popular metals used in the electrical

connectors and circuits, owing to its excellent electrical conductivity; however, it does not have very high strength [20]. It should be noted that high strength (or hardness) is warranted especially for connector applications, such as in button connectors, alligator clips, etc. If the size of these connectors is small (e.g., < 10 mm), then these can be readily fabricated from the HPT-processed disks or ECAP-processed bars and billets. It should be ensured that the electrical conductivity of Cu should not only remain high (i.e., as close to the annealed state as possible), but should also not deteriorate during service (i.e., equivalently, during room temperature ageing). Nevertheless, a limited number of reports have focused on the above challenge of obtaining high hardness-high conductivity in Cu processed by HPT [20-22].

Accordingly, one of the aims of this work is to evaluate the effect of HPT on the hardness, electrical resistivity (or conductivity) and fatigue behavior of commercially pure CP Cu, which is a better contender to be used in connectors as compared to high purity Cu, due to its inherent higher strength and better microstructural stability. The CP Cu disks were processed to very high HPT turns (of 50) at 6 GPa pressure and room temperature and stored under the ambient condition for 1.75 years to observe the effect of natural ageing on hardness as well as electrical resistivity of these samples. Hardness and electrical resistivity of these samples was measured as a function of the distance from the disk center to determine the HPT strain-property variations. In addition, a detailed analysis of microstructure was performed to gain important insights into processing-structure-property relationships. This report demonstrates the feasibility of using HPT for enhancing the hardness of CP Cu without significantly affecting its electrical conductivity and also comments on the effect of natural ageing on the hardness as well as on the resistivity of the Cu. In addition, although the fatigue response of the single crystal Cu [25-29], as well as polycrystalline Cu [30, 31], has been well studied, only a few studies have been reported on fatigue behavior of the HPT processed Cu [32]. So, here, we have also studied the fatigue behavior for the HPT processed Cu and compared it with the annealed Cu. Relevant microstructural characterization was performed using the electron back scattering diffraction (EBSD), scanning electron microscope (SEM) and transmission electron microscopy (TEM).

2. Literature Survey

2.1 Effect of HPT on microhardness

Many reports have been published on the effect of HPT on the microhardness of different metals and alloys [14, 15, 33]. Kaveh et al. [20] reported that the hardness value of high purity Cu (99.99%) gradually increases and gets saturated at a value of 132 HV after the HPT processing (room temperature, 2 GPa pressure, 0.5 rpm), as shown in **Figure 3**. They also observed that hardness value gets steady at 80 and 86 HV even after the post HPT annealing at the temperatures of 433 and 513 K, respectively.

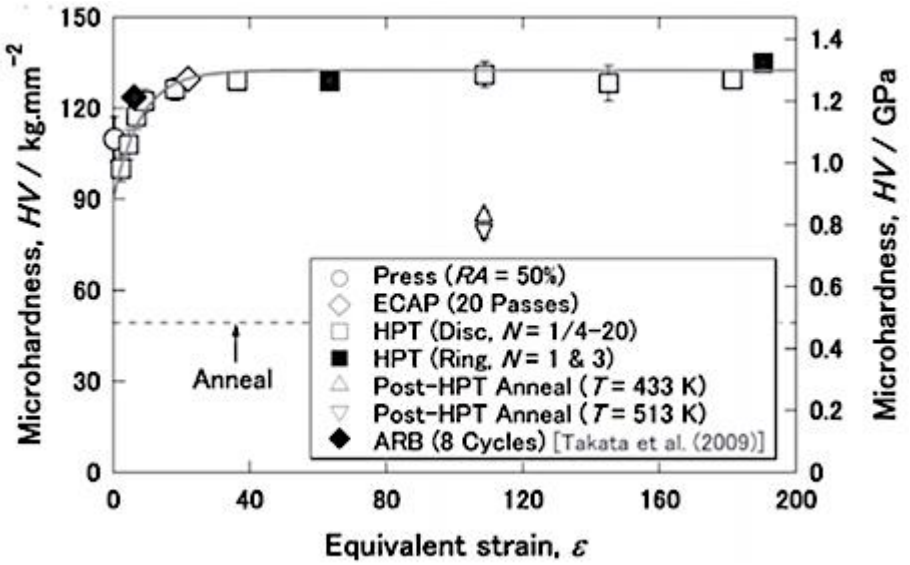

Figure 3: Variation of microhardness of high purity Cu, processed through HPT at different number of turns (0.25-20), with respect to equivalent shear strain [20].

Kaveh et al. in another report [34] studied the effect of HPT on the microhardness of Al and observed different trends than that of Cu. Microhardness attains the maximum value after initial increment with the progress of strain and then decreases with the further progress of the strain and finally attains the steady value as shown in **Figure 4**. Al is a FCC metal with a high value of the stacking fault energy; as a result, it is easy for the cross-slip. On the other hand, softening may happen dynamically during HPT processing, as suggested by Xu et al. [35], which is strikingly different than behavior of Cu.

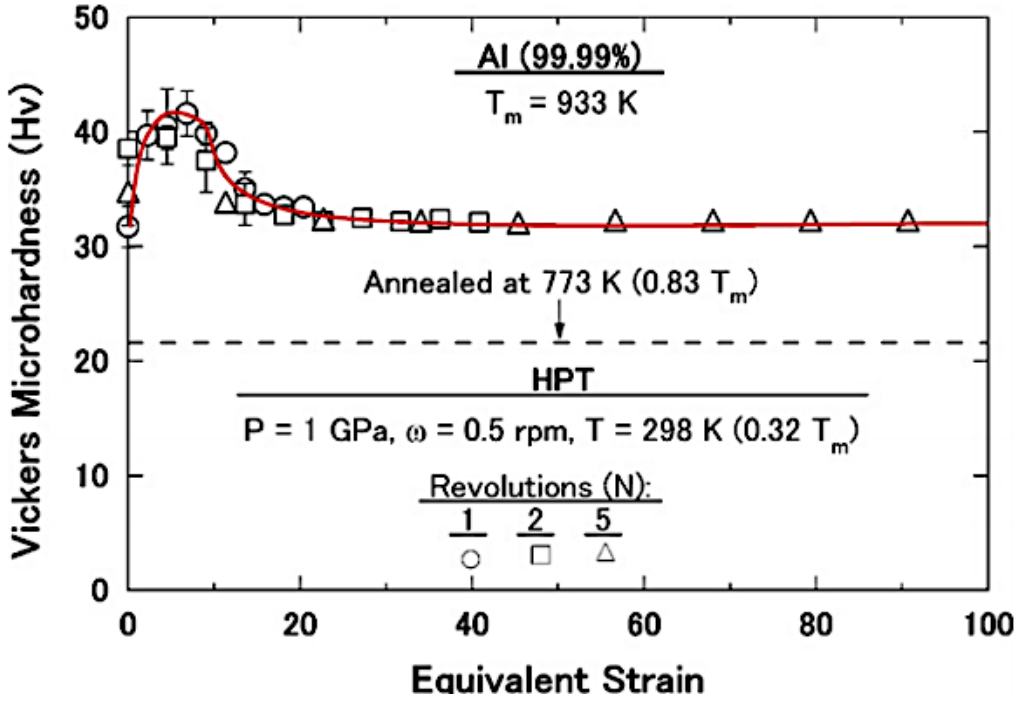

Figure 4: Variation of microhardness with respect to equivalent shear strain in high purity Al processed by HPT for 1, 2 and 5 numbers of turn (1GPa, 0.5rpm) [34].

Only a few studies have reported the effects of long-term natural ageing on HPT processed Cu samples [36, 37]. Almazrouee et al. [37] reported that there is a decrement in the hardness value of the OFHC Cu due to effect of ambient ageing. However, it should also be noted that since HPT processing also induces a significant strain (about 1000) with strain gradient along radial direction while also applying large compressive pressure, the samples are expected to incur a large amount of residual stresses. There is no report on the effect of residual stress on the microhardness value.

Hence in this report, we studied the effect of HPT, including the effect of subsequent long-term natural ageing, on the microhardness of the commercially pure Cu, which has more usability. In addition, we have also investigated the effect of microstructure and residual stress on the observed trends.

2.2 Effect of HPT on electrical resistivity

Limited studies have reported effect of HPT on the resistivity of Cu. Zhilyaev *et al.* [22] reported a maximum value of ~27.0 nΩ-m for the resistivity of machined chips of CP Cu, following consolidation using HPT performed at 6 GPa for 5 turns. They also suggested that phonon-electron scattering due to lattice distortion or defect might be reason for such

variation of resistivity. Moreover, Zhilyaev *et al.* [21] also obtained a value of electrical resistivity of ~25.0 nΩ-m for CP Cu samples processed at 6 GPa to 5 turns of HPT. Edalati *et al.* [20] studied the resistivity variation of the high purity Cu processed through HPT (1/4 to 20 turns) at 2 GPa. They observed that resistivity values increased with initial straining and saturated on further straining, as shown in **Figure 5**. The maximum increment in the resistivity value was 12% as compared to the value of annealed Cu. They also observed that 97% of the conductivity of the annealed copper can be retained after post-annealing of the HPT processed Cu.

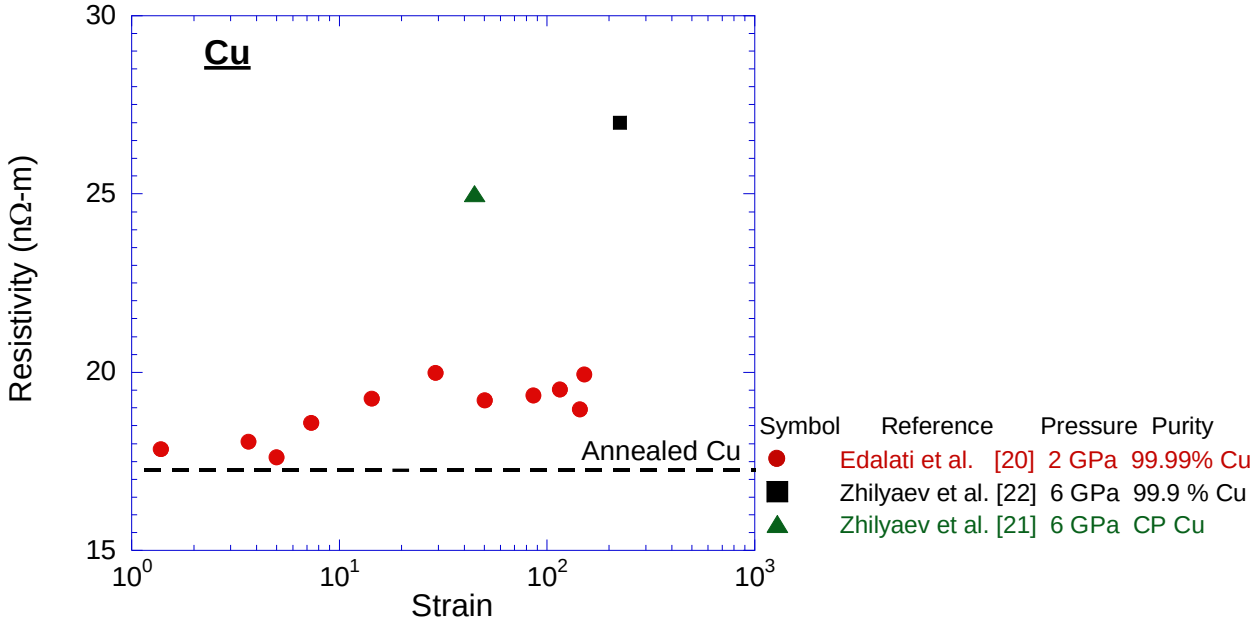

Figure 5: Variation of the electrical resistivity of HPT processed on Cu as function of the strain imposed during HPT. The datum points reported by Edalati et al. [20], who performed HPT for ¼ to 20 turns, Zhilyaev et al. [21], who performed HPT for 5 turns on CP Cu and Zhilyaev et al. [22], who performed HPT for 5 turns on the machined chips of CP Cu.

The resistivity values were measured in the above studies using larger sized or bulk samples, for example, a 4 mm long stripe was used by Edalati *et al.* [20]. In HPT, we know that there is a gradual variation of the properties as we move from center to the periphery radially. So, the value of resistivity that is measured in the case of large or bulk samples is actually the average resistivity value. In this study, we build a customized resistivity measurement set up to capture the local variation of resistivity within the range of 1 mm strips. Further, we conducted an in-depth analysis of the resistivity variation in relation with microstructure evolution, grain size, and grain boundaries. In this report, we also discuss the

effect of residual stresses as well as the effect of natural ageing on the electrical resistivity variation on the HPT processed sample, which are not yet reported in literature.

2.3 Effect of HPT processing on the fatigue behavior on Cu.

Fatigue behavior of the single crystal Cu is well studied, and it is established that veins and persistence slip bands (PSBs) are formed during fatigue of the single crystal Cu [25, 26] (see **Figures 6a** and **6b**). Many studies are available on the fatigue behavior of polycrystalline Cu [30, 31] as well. It is observed that PSBs can be observed in polycrystalline Cu depending upon the grain size and the strain attained during fatigue in these samples (See **Figure 6c**) [30]. However, sometimes it is difficult to observe PSBs in polycrystalline Cu, especially when the grain size is small, and only a distinct wall of dislocations could be observed with moderate spacing, e.g., sub-micrometer at plastic strain of ~10^{-3} (e.g., see **Figure 6d**) [31].

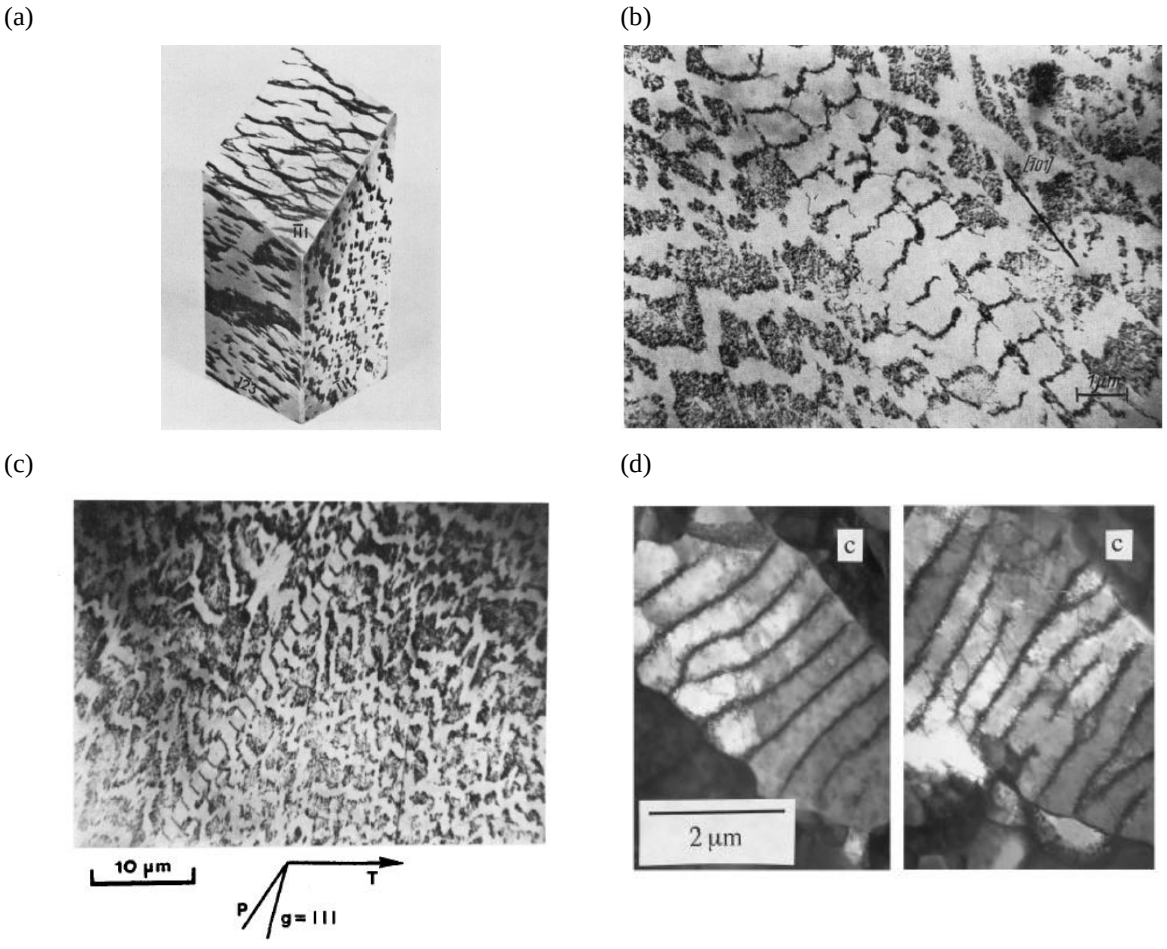

Figure 6: Example of dislocation substructures formed in Cu due to fatigue loading: (a) Early dislocation substructure, often termed as veins, formed in Cu single crystal [45]. (b) Veins and PSB substructures (at a depth of 50 μm below the (1-21) surface) in single crystalline Cu [46] (c) Vein and PSB substructures in polycrystalline Cu fatigued with low plastic strain amplitude [47]. (d) A primary dipole structure formed in a polycrystal after saturation in plastic strain [31].

It is generally understood that UFG materials have better fatigue resistance as compared to coarse grained materials under high cycle fatigue (HCF) regime due to their higher strength (as per Basquin rule); however, they show inferior resistance to low cycle fatigue (LCF) due to the poor ductility (as per Coffin–Manson rule). It is imperative, hence, to study fatigue response of UFG materials in under HCF regime. Khatibi *et al.* [32] studied the fatigue behavior of coarse-grained Cu and HPT processed Cu. They reported that HPT processed materials exhibit better high cycle fatigue life; however, they are susceptible to an increased crack propagation once the crack is formed. This indicates that ultrafine grained materials provide better resistance to the initial crack formation and a lower resistance against crack propagation, in comparison to the coarse-grained material. Only a few studies have reported the mechanism of nucleation of fatigue crack in the HPT processed sample in terms of the dislocation loop, mechanism of dislocation dipole, veins, and PSBs. Agnew *et al.* [31] reported the fatigue behavior of ultrafine grain Cu. They observed that extrusion and intrusion were formed at surfaces, as shown in **Figure 7** TEM images of the surface interior did not reveal PSB formation. A skeptical question arises whether there is the formation of PSBs or not in finer grain sized materials. It is reported that grain size is much smaller than what is required for the PSBs formation and there is an abundance availability of defects present in the ultrafine grained materials [31]. In this report, we analyze the nature and mechanism of extrusion and intrusion formation in the fatigued HPT and annealed Cu sample. An attempt is also made to characterize the dislocation structure of fatigued and annealed Cu.

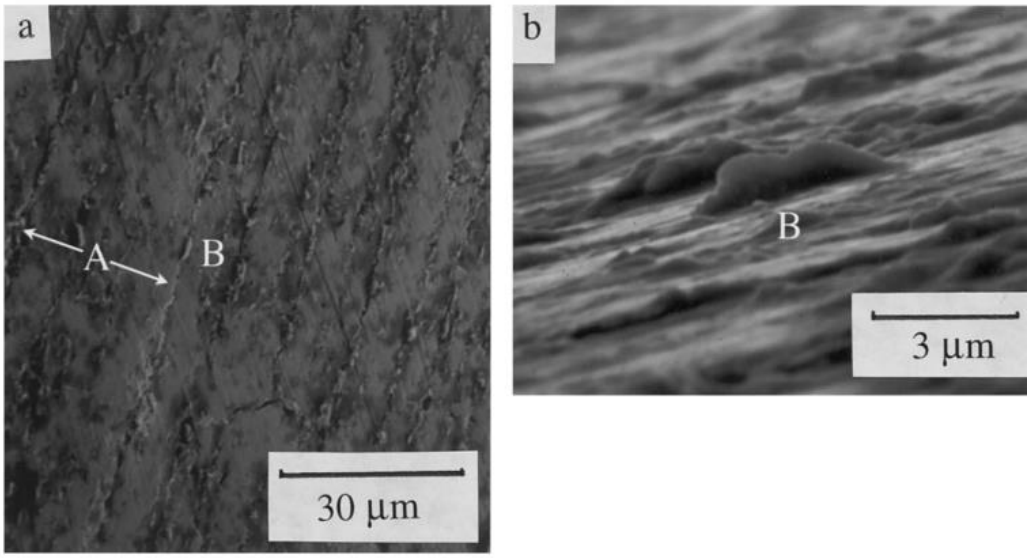

Figure 7: TEM micrographs showing (a) instances of formation of extrusion and intrusion on the surface of UFG Cu after imposing low strain amplitudes during fatigue, and (b) tilted view showing protrusions at location B marked in (a) [30].

3. Experimental Procedures

In this study, commercially pure Cu was selected as a model material. It is one of the easily available material that also possesses an excellent electrical conductivity; however, it suffers from relatively low mechanical strength and hardness. Therefore, we studied how its properties, such as electrical resistivity, microhardness and fatigue behavior, would be affected by the HPT processing. Also, given the utility of this material in electrical applications, we also comment on how to achieve an optimum combination of desired properties without hampering others.

3.1 HPT Processing

A commercially pure electrical grade of Cu was machined into disks of 10 mm diameter and 1 mm thickness, which were then isothermally annealed at 600 ^{o}C for 1 h for homogenizing the microstructure and removing residual stresses induced due to the machining. The disks are then thinned down to a final thickness of 0.85 mm.

There are three types of HPT setup, namely (i) unconstrained HPT, where sample is free to flow out of the anvil during the processing (**Figure 8a**) and hence, there is no control over the diameter of the specimen, (ii) constrained HPT, where there is no allowance for the diameter to increase during compression (**Figure 8b**) and (iii) quasi-constrained HPT, where there is limited outflow of the material through the anvil due to compression (**Figure 8c**). In this study, quasi-constrained HPT processing was conducted by placing the annealed, disc-shaped samples in between the two anvils with slight intrusion in the central region and by rotating the upper anvil while a compressive pressure of 6 GPa was applied on to the anvils[1]. The high compressive pressure ensured no slipping between the surface of anvils and the sample. The samples were processed for the following number of rotations: ¼, ½, 1, 5 and 10 for evaluating effects of HPT processing, i.e., without natural ageing, on microhardness, electrical resistivity and fatigue response of Cu, and for ½, 10, and 50 turns for observing the effect of long term (1.75 years) ageing at room temperature, i.e., natural ageing, on microhardness and electrical resistivity.

[1]All HPT processing was conducted at the facility hosted by Professor Megumi Kawasaki at Department of Mechanical, Industrial and Manufacturing Engineering, Oregon state University.

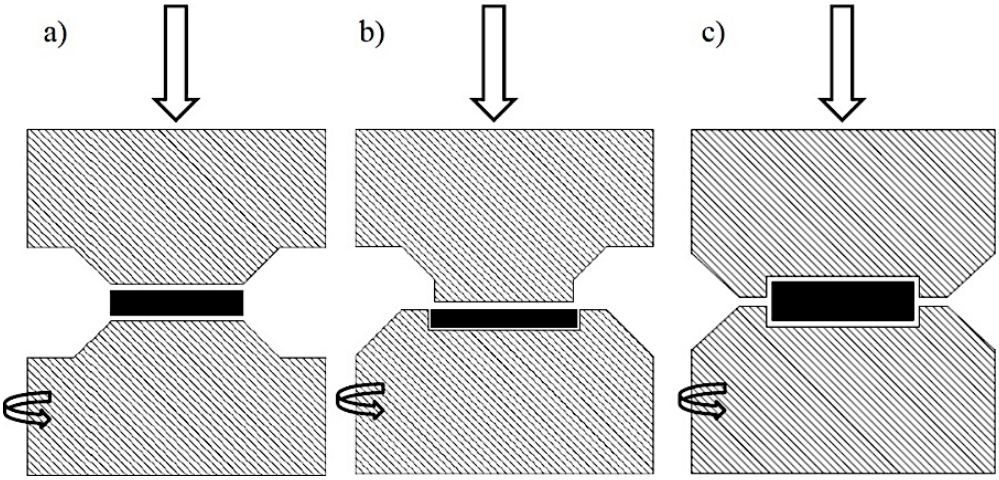

Figure 8**:** Schematics showing different HPT processing configurations: (a) unconstrained, (b) constrained and (c) quasi-constrained [38].

3.2 Microhardness and Microstructure analysis

Hardness of the samples was measured using a Vickers micro-hardness tester with a pyramid-shaped diamond indenter. Prior to the micro-hardness measurements, one of the flat surfaces of samples was metallographically polished up to 50 nm surface finish using colloidal silica. Vickers micro-hardness testing was performed by applying a load of 100 g onto the polished samples for 15 s. Numerous indentations were made onto a sample along two perpendicular diameters in a fashion schematically illustrated in **Figure 9**. As shown in **Figure 9**, for the collection of the data at a point, 5 measurements were taken at and around the point, respectively. Each indent was separated by a distance which is greater than 2.5 times the diagonal of the indent from the nearest indents to avoid any effect of the cold work from the previous indentation. Hence, as per the schematic shown in **Figure 9**, a total of 20 indents were made for a given magnitude of the radial distance (or equivalently a strain – see Eq. 1). The results of all these 20 measurements were averaged to calculate the representative hardness values as a function of r, thus an equivalent strain by HPT (except $r = 0$ for which only 5 datum points could be obtained). In this study, this average hardness value will be reported along with an error bar showing the standard deviation of all datum points used to calculate the average hardness. One may refer to [5] for the details of the aforementioned procedure for measuring hardness.

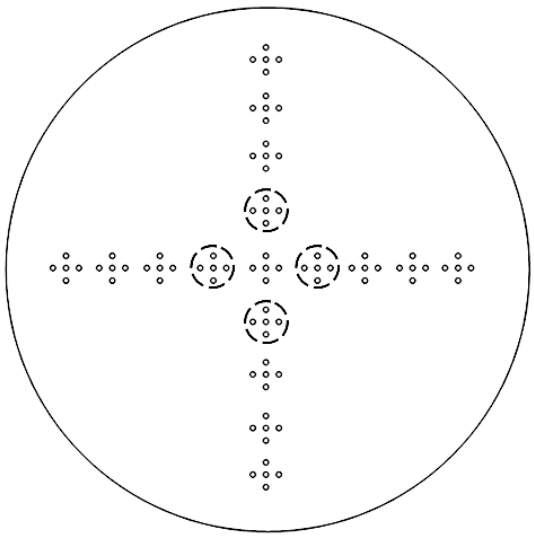

Figure 9: A schematic illustration showing the procedure followed in this study for performing micro-hardness tests using Vickers hardness tester. For illustration purpose, a group of 5 points corresponding to a point in the radial direction is inscribed by circles with dashed boundary. The radial distances of the representative points were 0, ± 1, ± 2, ± 3 and ± 4 mm away from the center of the disk, along each diameter.

Microstructural analysis was performed using EBSD on the metallographically polished Cu samples before and after processing by HPT. For EBSD, the metallographically polished samples were further electro-polished using the standard D-2 electrolyte solution, which is prepared by mixing 40% phosphoric acid, 25% ethanol, 5% propan-1-ol, 29% water and 1% urea. The Cu sample, which was connected to the cathode, and the steel anode were dipped into the electrolyte, which was constantly agitated using a magnetic stirrer and was maintained at 5 ^{o}C. An optimized combination of voltage and current of 25 V and 0.7 A, respectively, were applied for 10 s to obtain a mirror-finished surface required for the EBSD analysis. EBSD analysis was conducted at different regions of the disk samples to evaluate the effect of HPT strain on the microstructure and texture. For EBSD analysis, a step size of 50 nm was used for ultra-fine grains, whereas a step size of 1 μm was used for the coarse-grained sample (i.e., unprocessed sample). Any misorientation exceeding 5^{o} was considered as a boundary to quantify the grain size, whereas a misorientation angle of 15^{o} was used to distinguish between a high angle boundary and a low angle boundary. Grain sizes of the materials were measured by a mean linear intercept method using OIM software®.

3.3 Electrical resistivity measurement

For measurements of electrical resistivity, the Cu disk samples were firstly mounted in polymer resin and then metallographically polished up to 50 nm surface finish using

colloidal silica. At the end of this process, the thickness of the samples was reduced to 0.5 mm. A thin strip of approximately 1 mm width and 10 mm length along one of the diameters of the sample was cut from each resin-mounted sample using a low-speed diamond saw. This strip was again sliced into 5 pieces of equal lengths. These sliced pieces were removed from polymer resin by dissolving the later in acetone.

A setup was designed and fabricated to measure the electrical conductivity of miniaturized Cu samples using the standard four probe method; the customized setup is schematically illustrated in **Figure 10a**. As shown in **Figure 10a**, firstly a sample was placed in between 2 high purity Cu blocks, which were then pushed onto the sample with the help of a screw attached to one of the Cu blocks (i.e., movable Cu block). The screw and the fixed Cu block were connected to an external high precision power supply. As shown in **Figure 10a**, a voltage drop between two points along the length of the sample was measured using 2 thin W electrodes, which were fixed on the outer sliders with the support of small screws. Once the electrodes were carefully placed on the top surface of the metallographically polished samples, they were connected to a nano-voltmeter for measuring the voltage drop with a resolution of 10 nV. These fine W electrodes were fabricated from a W rod of 1 mm diameter by grinding and chemically etching in HF and had a tip diameter of 50 μm. Since W has high stiffness and hardness, it could easily make a small indent into the top surface of the CP Cu samples, thereby enabling accurate measurements of the distance between the 2 points on the sample across which the voltage drop was measured, *l*, using an optical microscope. The distance between these 2 points was kept close to 1 mm.

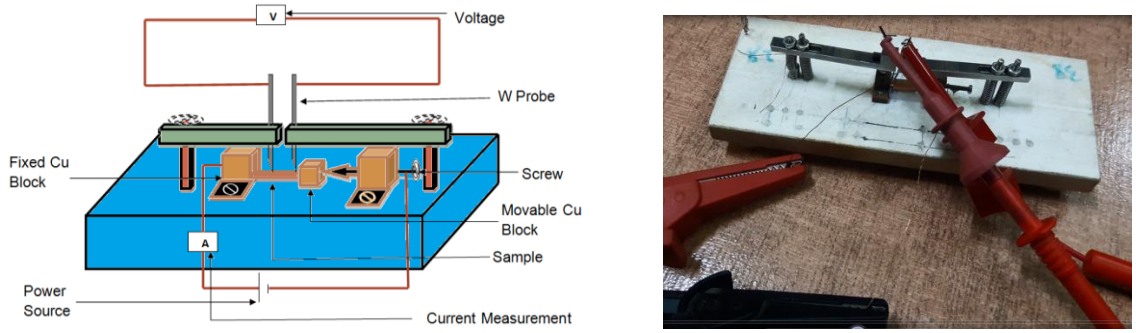

(a) **(b)**

Figure 10: (a) A schematic illustration of the test setup used for measuring the electrical resistivity of samples in this study and (b) pictograph of the measurement setup.

Once the hardware setup was completed, an electric current ranging from 0.1 to 0.9 A was passed through the sample and the corresponding voltage drop was measured. The voltage drop was plotted as a function of the applied current and the best-fit line was drawn,

whose slope was taken as the value of resistance of the sample, *R*, between the 2 points over which the voltage drop was measured. Subsequently, the resistivity of the sample,ρ was calculated using the following relation:

$$\rho = \frac{RA}{l} \tag{2}$$

where *A* is the cross-sectional area of the samples (through which a current of uniform density was passed). Validation of the aforementioned test setup and the procedure was performed by measuring and comparing the electrical resistivity, measured along with several directions, of coarse-grained CP Cu and CP Ni having the same dimensions as of the actual samples (i.e., 2 × 1 × 0.5 mm^3). The results are shown in **Figure 11** where the resistivity values of the CP Cu and CP Ni were measured as 17.3 ± 0.3 and 73.0 ± 3.0 nΩ-m, respectively, which were very close to their respective standard values of 17.2 [39] and 75.0 nΩ-m [40], respectively.

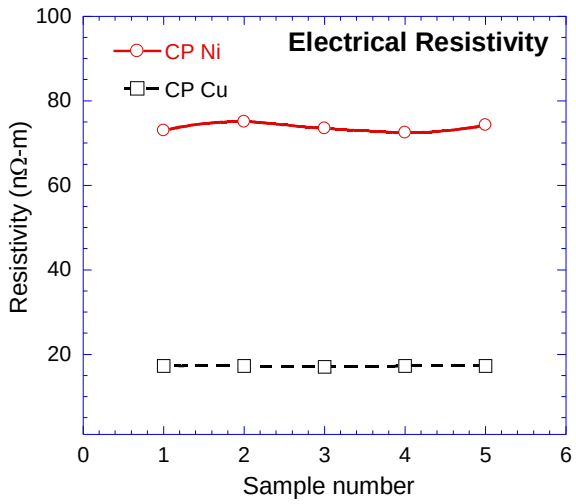

Figure 11: Validation of the accuracy of the measurement of resistivity using the setup by testing 2 commercially pure metals, whose electrical resistivity values were known.

3.4 Residual stress measurement

The samples cut for electrical resistivity measurements were also utilized to evaluate the residual stresses using x-ray diffraction (XRD). Prior to the XRD-based analysis, each small sample was mounted in an epoxy resin, which is an amorphous polymer. This mounting in the amorphous resin enabled fixing of such small samples on the x-ray diffractometer stage without interference or background from the Al stage of the diffractometer. A four-circle high-resolution x-ray diffractometer, with 0.015^o resolution, was utilized to conduct the x-ray measurements to calculate the residual stresses. A step size of 0.03^o was utilized to collect the data in the diffractometer. It should be noted that due to the residual stress in a material, the

original lattice spacing, d_0, changes and results in a different lattice spacing, d. Hence, to satisfy the Bragg's law for the new lattice spacing, the position of the XRD peak for a plane must shift. Hence, measurement of the peak shift, as compared to the unstrained sample, readily allows calculation of the residual stress. The maximum tensile or compressive residual stress, σ_{res}, is given by:

$$\sigma_{res} = E \frac{\Delta 2\theta}{4 \tan \theta} \tag{3}$$

where E is the elastic modulus of the material at the test temperature (which is equal to 128 GPa for Cu at room temperature), $\Delta 2\theta$ is the peak shift due to the lattice strain and tan θ is calculated from the reference annealed samples peaks [41]. It should be noted that all residual stress measurements in this study were performed at room temperature. The combination of x-ray wavelength, incidence and diffracted angle gave a penetration depth of only 4.46 μm and hence the measured residual stress is representative of top surface only.

3.5 Fatigue test

The fatigue tests were performed on annealed Cu sample and the Cu samples processed to 50 turns of HPT. Samples of specific dimensions (see **Figure 12)**, having a gauge length of 0.8 mm, were cut down using micro-electrical discharge machining (μ-EDM). In a consecutive process, all samples were electropolished in the gage section in order to eliminate thermally affected zones from manufacturing and to avoid the influence of surface defects on the damage formation by ameliorating surface quality. The fatigue setup[2] works at the resonance of the sample to achieve the required excitation amplitudes. The design allows torsional and bending modes in this setup as well. Thus, it is possible to perform fatigue by choosing a required frequency between these two resonant modes. However, all tests in this study were performed only in bending. The design of the resonant fatigue setup is shown in **Figure 13**. It contains two piezo actuators whereupon a flat spring is clamped. The actuation is implemented by two piezo stacks (P-843.40, Physik Instrumente, Germany). These piezo translators are high-resolution linear actuators suitable for static and dynamic applications. They provided the sub-millisecond time response necessary for kHz actuation. Each piezo actuator is attached with integrated high-resolution position sensors for accurate precision

[2]All Fatigue test were conducted at the facility hosted at the Fraunhofer Institute for Mechanics of Materials IWM, Freiburg, Germany. Thanks to Dr. Thomas Straub, Dr. Tobias Kennerknecht and Prof. Christoph Eberl for hosting Professor Praveen Kumar and helping him to perform the tests.

(linearity to 0.01 %, and a bandwidth up to 5 kHz). These sensors are used to capture the two piezo displacement signals, i.e., the exact setup input actuation. The spring can be bent slightly and/or twisted by the two actuators. Spring is made up of steel and selected in a way that the strain developed on the surface is always well below the fatigue limit while its resonant frequency is well above the sample resonant frequency. By this optimization, fatigue will never occur in the spring. The sample is attached to the end of the spring and is displaced out of the plane at its fixed end during bending actuation (this can be achieved by an in-phase excitation of the two piezo actuators). The displacement amplitude is captured using a laser beam. The beam gets reflected from the surface of the sample onto a detector. The area detector is a Position-Sensitive Device (PSD), and has a high-frequency analog data acquisition system, an update rate up to 30 kHz, and an optical resolution of 1 μm. The sensor can measure the bending and torsion deflection of the sample; i.e., the output oscillation [42].

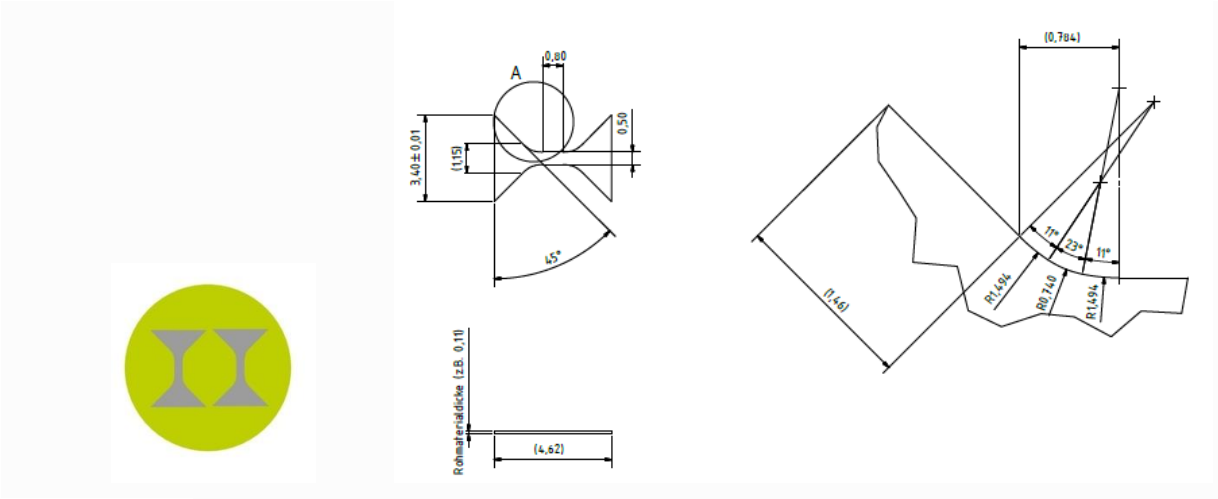

(a) **(b)**

Figure 12: (a) Schematic figure showing the sample cut down from the sample disc. (b) Sample geometry showing all the dimensions [42]. All dimensions are in mm.

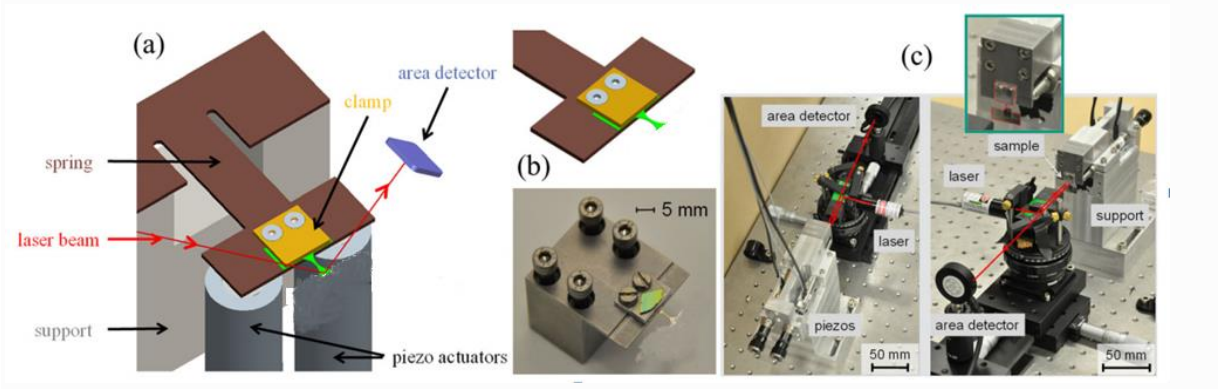

Figure 13: **(**a**)** Schematic showing the design of the setup. **(**b**)** Image showing the detail of clamp and sample holding. **(**c**)** Original picture of the setup. These pictures have been taken from PhD thesis of Dr. Thomas Straub.

The setup works at the resonance of the sample to achieve the required excitation amplitudes. As the fatigue progresses, it induces defects in the sample, which results in the decrease of the resonance frequency of the sample. The tests were stopped after a 20 % decrease in the resonant frequency, f, was observed (i.e., $\Delta f/f = 0.2$).

4. Results and Discussion

4.1 Microhardness variation

Two different types of samples were analyzed, one is as fabricated, i.e. tests were performed within 20 days from the fabrication and the other is natural aged samples which were kept at normal laboratory conditions for 1.75 years to study the effect of natural ageing on the HPT processed Cu. These results are discussed in the subsequent sub-sections.

4.1.1 As-fabricated sample

Figure 13 shows the variation of the Vickers micro-hardness as a function of the distance from the center of the commercially pure Cu disc after HPT for ¼, ½, 1 and 10 turns and with only 20 days of the natural ageing. These samples will be termed as "as-fabricated samples", as natural ageing was not significant.[3] As shown in **Figure 14**, the hardness of the annealed Cu, i.e., without HPT, was the minimum, equal to ~ 47 HV as shown by the dashed line. The hardness value at the center of the ¼ turn sample was 113 HV which gradually increased and attained a value of 145 HV at the periphery region. For the ½ turn sample, the hardness value at the center of the disc was about 128 HV, which subsequently reached the maximum value of 154 HV at the periphery after gradual increment away from the center. A similar trend was observed for 1 turn and 10 turns samples also, i.e., the hardness values at the central region were 129 HV and 140 HV for the respective turns, whereas they got saturated at 150 HV for the 1 turn and 155 HV for the 10 turns samples in the periphery region. It shows that hardness in the center region was generally smaller than the value in the periphery region; this trend of generally expected, as the strain imposed onto the disk samples during HPT processing is smaller in the central region than that in the periphery (see **Equation 1**). So due to the more straining, grain size at the periphery gets more refined than that in the center

[3] Except for the instances of the samples being in shipping (from Oregon to IISc, and then to and fro between IISc Bangalore and IIT Bombay) and metallographically polished and characterized, they were stored in deep freezer (~-70 ^{o}C). 20 days is the estimated time for it being in the ambient conditions (i.e., except for the time it was stored in deep freezer).

region. According to the Hall-Petch relation, smaller the grain size is the higher is the strength [43]. Interestingly, for the 10 turns sample, there might not much variation in the hardness value in the center and the periphery regions; this indicates that there was more homogeneity in the microstructure in 10 turns samples as compared to the samples processed to less number of HPT turns. This will be confirmed later.

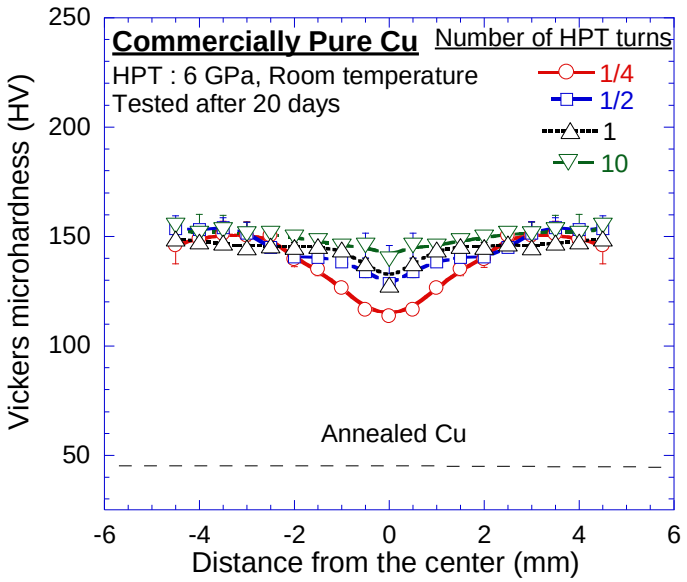

Figure 14: Variation of micro-hardness of CP Cu as a function of radial distance away from the center for the as-fabricated samples. The hardness profile was radially symmetric and each datum points here corresponds to 10 readings.

4.1.2 Naturally aged samples

Figure 14 shows the variation of the hardness as a function of the distance from the center of the HPT processed CP Cu disks after annealing for 1.75 years of storage under ambient conditions or natural ageing. The hardness of the coarse-grained Cu, i.e., without HPT but annealed for 1.75 years along with HPT processed samples, was the minimum, equal to ~ 48 HV with a little variation across the sample, of all the samples. **Figure 15** also reveals that the hardness of CP Cu samples increased with HPT processing; however, the difference between the samples processed through 10 and 50 turns was marginal. The hardness at the center of the sample processed to 10 turns of HPT was ~130 HV, which then gradually increased to 140 HV near its periphery. On the other hand, the hardness of CP Cu increased to ~155 HV throughout the sample after 50 turns of HPT. This, along with the results obtained on the as-fabricated samples, confirm the homogenization of the microstructure throughout 10 mm diameter disks once a certain strain was imposed through HPT. A similar trend was

observed in other FCC metals, where the hardness of materials showed a saturation in the value after a large number of HPT turns [9, 30-32].

However, the hardness profile of the Cu sample processed to ½ turn of HPT followed by ambient aging was noticeably non-uniform. In practice, the value of micro-hardness in the center was ~120 HV, which gradually increased to a value of ~135 HV at a distance of 1 mm from the center; notwithstanding, the hardness sharply dropped to a value of only ~80 HV at a distance of 2 mm from the center before finally attaining a value of ~90 HV near the periphery of the sample. Such a variation in ½ turn data is consistent with the literature on HPT processed–ambient aged Cu [33, 34], while it is quite different than the hardness variation of CP Cu immediately after HPT (as-fabricated sample – see **Fig. 14**).

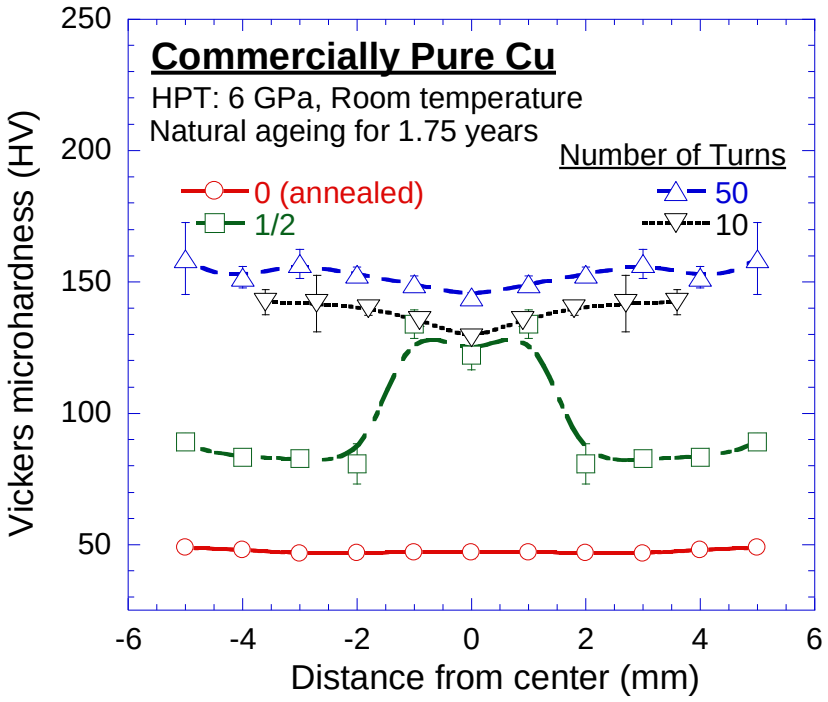

Figure 15: Variation of micro-hardness of CP Cu as function of radial distance away from the center for the HPT processed samples naturally aged for 1.75 years. The hardness profile was radially symmetric and each datum points here corresponds to 10 readings.

4.1.3 Comparison of the as fabricated samples and naturally aged sample

Figure 16 shows the variation of the hardness of CP-Cu as a function of the equivalent strain imposed by HPT, as given by **Equation 1,** for both as-fabricated samples and naturally aged samples. For ease of representation of the data, the strain in **Figure 16** is shown on a log-axis and hence the hardness data of the coarse-grained sample without HPT (i.e., equivalent von Mises strain, $\varepsilon_{ev} = 0$) is shown by a horizontal broken line at ~47 HV in the

plot. **Figure 16** reveals that the hardness of the CP Cu for the as-fabricated sample reached the value of 113 HV at the initial strain value of 0.4 and its value gradually increased and reached saturated value of ~150 after the strain value of 2.2. However, for the naturally aged sample, the hardness value increased to ~135 HV at the onset of the HPT processing (i.e., ε_{ev} = 1.8), followed by a rapid decrease to a value of only ~ 80 HV at an equivalent strain of 3.6. Thereafter, the hardness value increased rapidly up to a value of 135 HV and gradually increased to a value of ~160 after a strain of ~900. The sharp drop in hardness followed by a rapid increase in the very early stage of torsion straining becomes apparent in the semi-log plot, while a conventional display of the hardness changes in a linear-linear graph fails to reveal such hardness change in an earlier stage of the plastic deformation in the Cu samples.

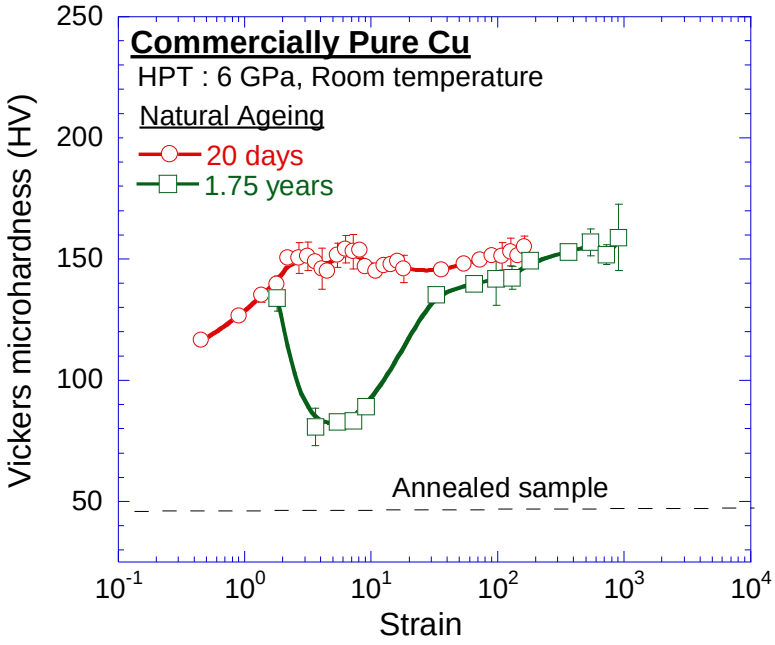

Figure 16: Variation of micro-hardness of CP Cu as function of the effective strain imposed during HPT processing.

If the as-fabricated sample and the naturally aged sample are compared, ½ turn sample and 10 turns sample are common in both the sample fabrication conditions. So, it can be observed that for the 10 turns sample, there was no change in the hardness value for both the central and the periphery regions due to the prolonged natural ageing. However, for the 1/2 turn sample, hardness value at the periphery region drops down significantly after prolonged natural ageing, whereas hardness value at the center region remains almost the same. In summary and as shown in **Figure 16**, HPT processed-naturally aged sample showed a good match with the "as-fabricated" sample, except for unexpected "drop" in hardness in

samples at small strains (2-10). The effect of natural ageing is observed to be dominated only in the small strain region of (2-10).

The variation of hardness was plotted with respect to distance away from the center for the 1/2 turns sample at the different ageing time (see **Figure 17)**; the data are collected from the literature [36, 37] and present work. **Figure 17** consistently shows a pronounced effect of natural ageing on the hardness evolution of CP Cu samples: The sample which is just 20 days aged shows more hardness at the periphery region, i.e., 155 HV, as compared to the central region, i.e., 128 HV. As the time of ageing increased to 6 weeks, hardness value in the periphery region dropped down to a value of about 80 HV.

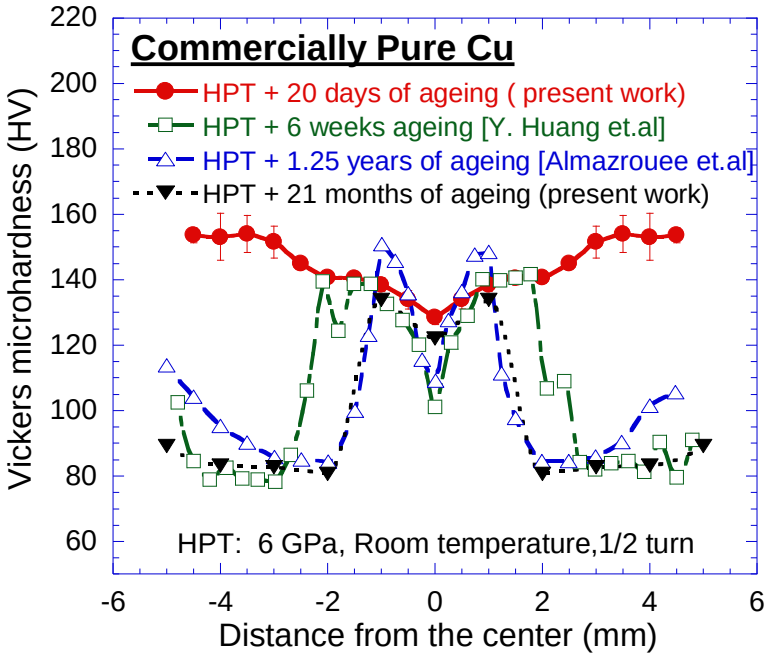

Figure 17: Variation of micro-hardness of CP Cu as function of radial distance away from the center for the as-fabricated samples for the 1/2 turn sample for the different ageing time. The hardness profile was radially symmetric.

4.2 Microstructural characterization

Figure 18 shows a representative inverse pole figure (IPF) of the annealed coarse-grained Cu sample, suggesting that the crystallographic texture of the annealed sample was random. Although the fraction of (101)-orientated grains in this particular IPF map was lesser than other major orientations, the examination of other IPF maps did not reveal the dominance of any one particular crystallographic texture. The grain size of the annealed Cu was measured as ~11±2 μm. It also reveals the presence of annealing twins in the annealed Cu samples.

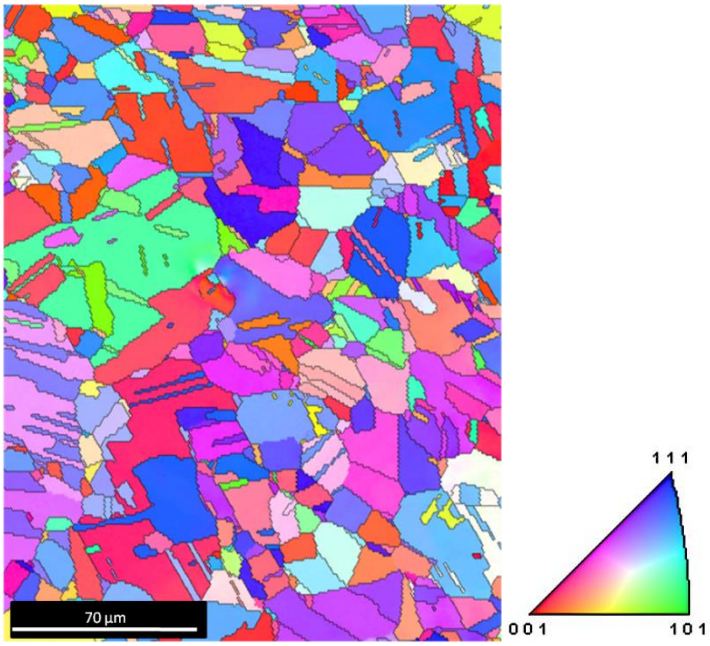

Figure 18: An example inverse pole figure (IPF) map of annealed coarse-grained Cu, showing the grain structure and the distribution of crystallographic orientations. The legend on the right show the color map for IPF.

4.2.1 Effect of HPT on microstructure of as-fabricated sample

Figure 19a-c show a series of IPF maps taken at various locations (e.g., r = 0, 2.25 and 4.5 mm) in the as-fabricated CP Cu sample processed for ¼, ½ and 10 turns, respectively. The microstructures do not show any preferred crystallographic texture. Microstructure for the ¼ and ½ turn samples shows more heterogeneity, and a well identifiable variation in the microstructure form center to the periphery is evident in both samples. On the other hand, grains were homogeneously distributed in 10 turns sample and there was no distinct variation in the microstructure from center to the periphery; this clearly indicates that the microstructure in the disks became saturated after 10 turns of HPT processing.

Figure 20 shows the grain size distribution of the as-fabricated HPT samples processed through ¼ and ½ turns. It should be noted that grain size was measured by using the line intercept methods. The distribution shown in **Figure 20** was plotted with number fraction as the y-axis and intercept per line length as the x-axis. Grain size distribution shows the heterogeneity and Gaussian, or natural-log distributions types of standard distribution was not observed. The Gaussian distribution generally indicates that data is symmetric about the mean value and data near the mean value is the more frequently occurring data than the other data away from the mean value. In such a case only, a meaningful average number can be defined. However, the grain size distribution became closer to Gaussian distribution with an

increase in the strain (not shown here), and overall an average grain size was defined for all cases (even at low strains, where they do not carry the same significance).

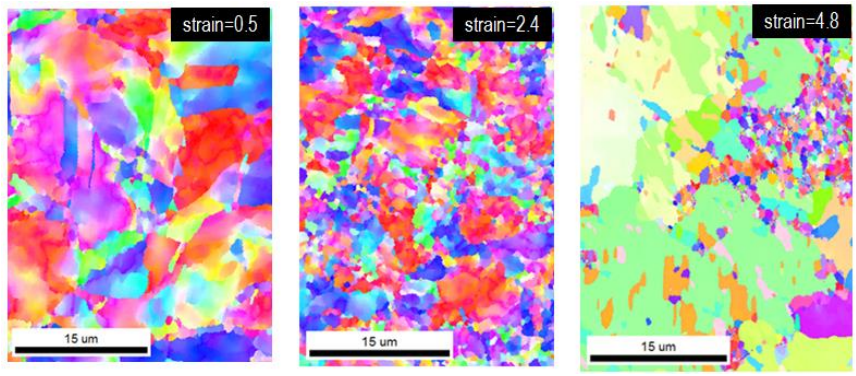

(a)

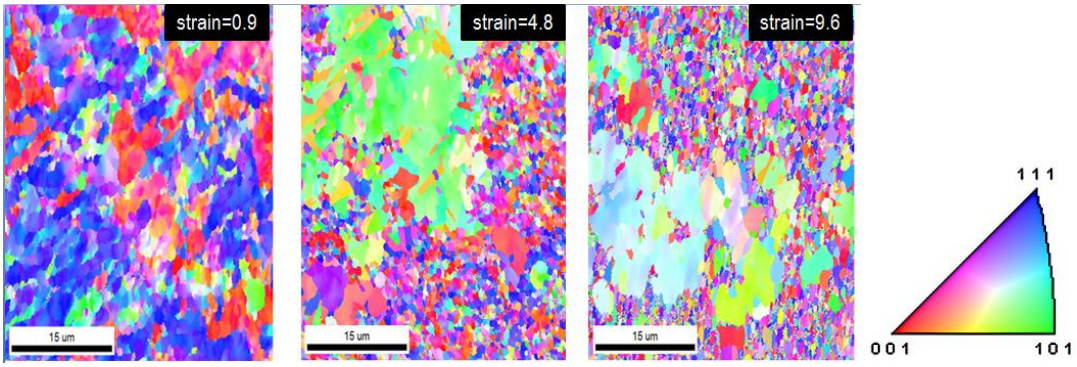

(b)

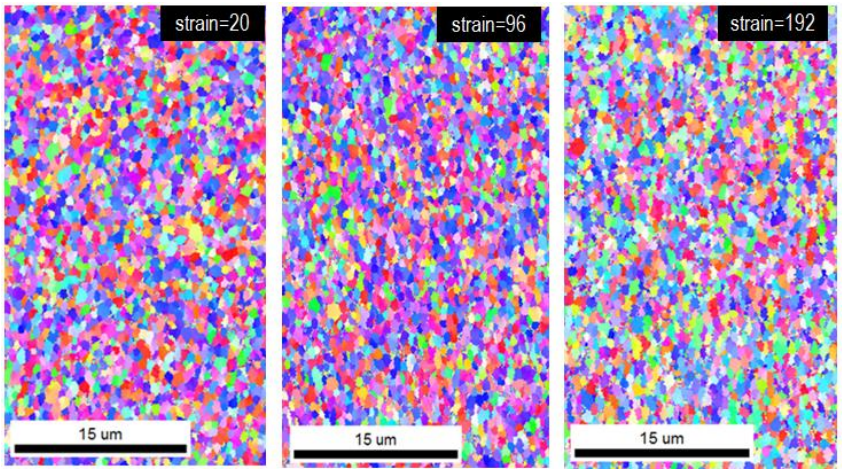

(c)

Figure 19: Inverse pole figure (IPF) map of fabricated sample locations of r = 0 mm, 2.25 mm, 4.5 mm (a) ¼, (b) ½ and (c) 10 turns.

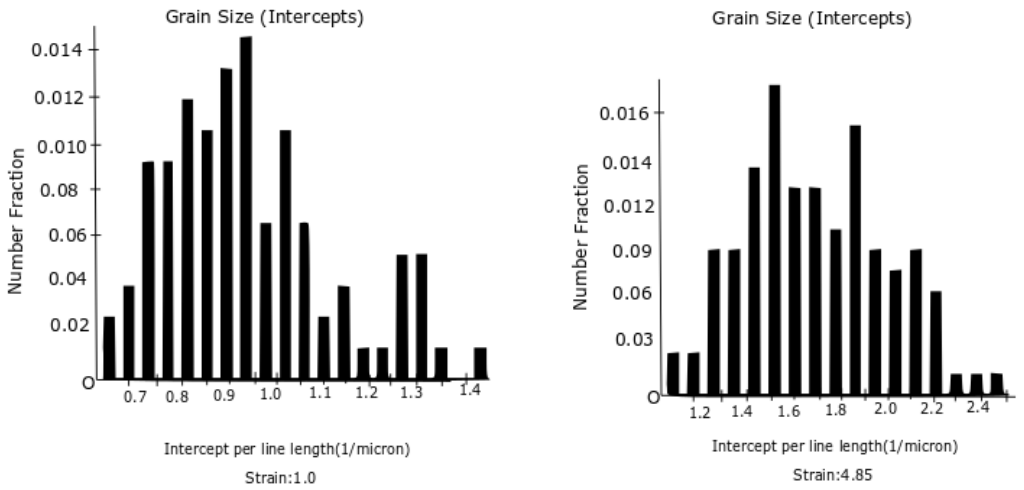

Figure 20: Histograms showing the grain distribution in as-fabricated sample processed up to a strain of (a) 1.0 and (b) 4.85 strains in the disk processed to ½ turn of HPT.

4.2.2 Effect of natural ageing on HPT processed sample

Figure 21 shows a series of IPF maps taken at distances of r = 0.6, 2.0, 3.2 and 4.2 mm away from the center of the disk of the CP Cu sample processed for ½ turn of HPT followed by the ambient aging for 1.75 years. The non-monotonous variation in the grain size, as shown in **Figure 21**, can explain the non-uniform hardness profile for this sample as shown in **Figure 15**. The microstructure shown in **Figure 21** also does not show any preferred texture.

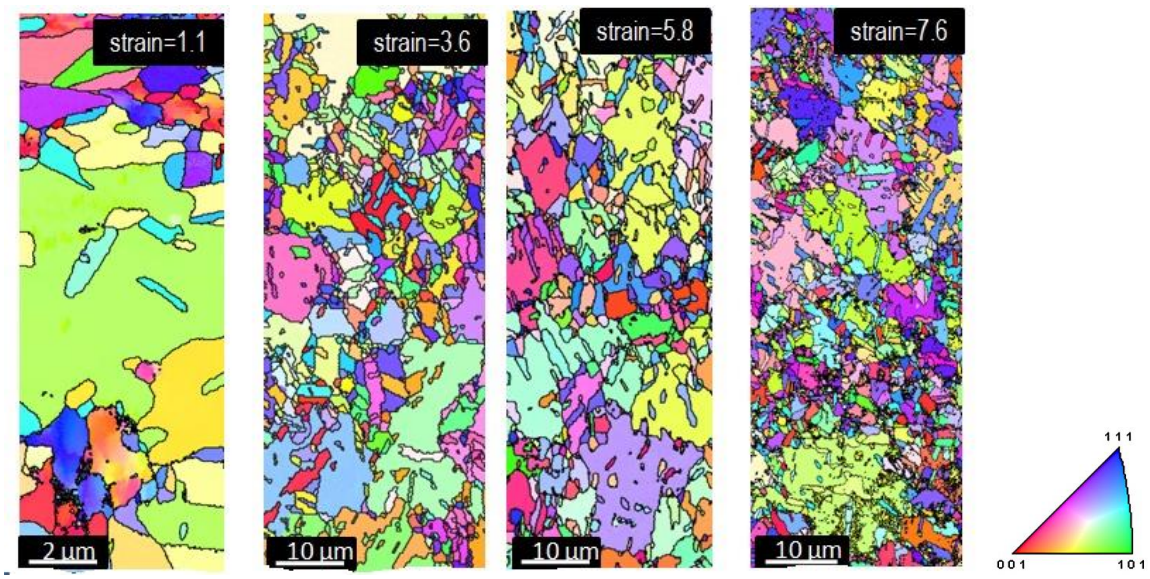

Figure 21: Inverse pole figure (IPF) map of naturally aged sample processed up to ½ turn: The effective strains are mentioned on top right corner of each map, which correspond to different radial distances of r = mm, 2.0, 3.2 and 4.2mm (from left to right).

Figure 22 shows the IPF maps taken at (a) 1.0, (b) 3.0 and (c) 4.2 mm away from the disk center after HPT for 10 turns and **Figure 23** shows the IPF maps taken at (a) ~0.1, (b) 4 and (c) 4.5mm from the disk center after 50 turns of HPT (followed by natural ageing). A comparison of **Figures 22a-c** and **23a-c** reveals an insignificant change in the size and morphology of grains with the distance from the center of the CP Cu disks processed through ≥ 10 turns by HPT. Moreover, as revealed from a comparison of **Figures 23a** and **23b-c (**and **22a-c),** the morphology of grains in the locations away from the central regions was slightly elongated; this may be attributed to the rotational shear associated with the HPT processing. Overall, these CP Cu disks after HPT for 10 and 50 turns demonstrated random crystallographic texture.

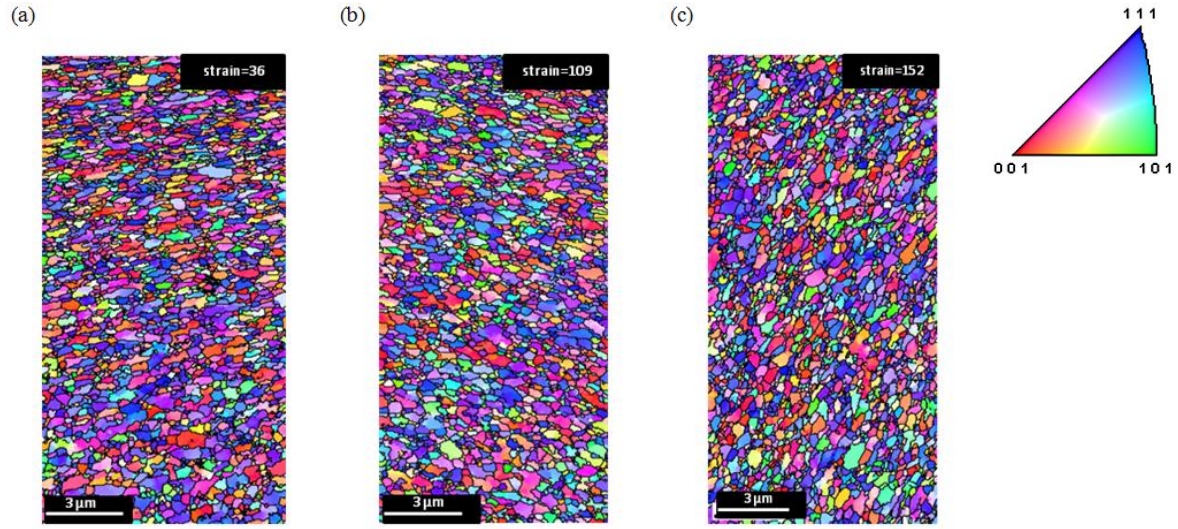

Figure 22: IPF maps showing various locations in the CP Cu disk processed up to 10 turns of HPT: The average radial distance of each location was (a) 1, (b) 3 and (c) 4.2 mm from the center. The corresponding average strain value is shown in the top-right corner of each IPF map.

Figure 24 shows the grain size distribution of the naturally aged HPT sample processed up to ½ turn. It is observed that heterogeneity decreased with prolonged natural ageing and distribution became closer to the Gauss distribution, especially at higher strains as compared to the ½ turn sample in the as-fabricated condition (see **Figure 20**).

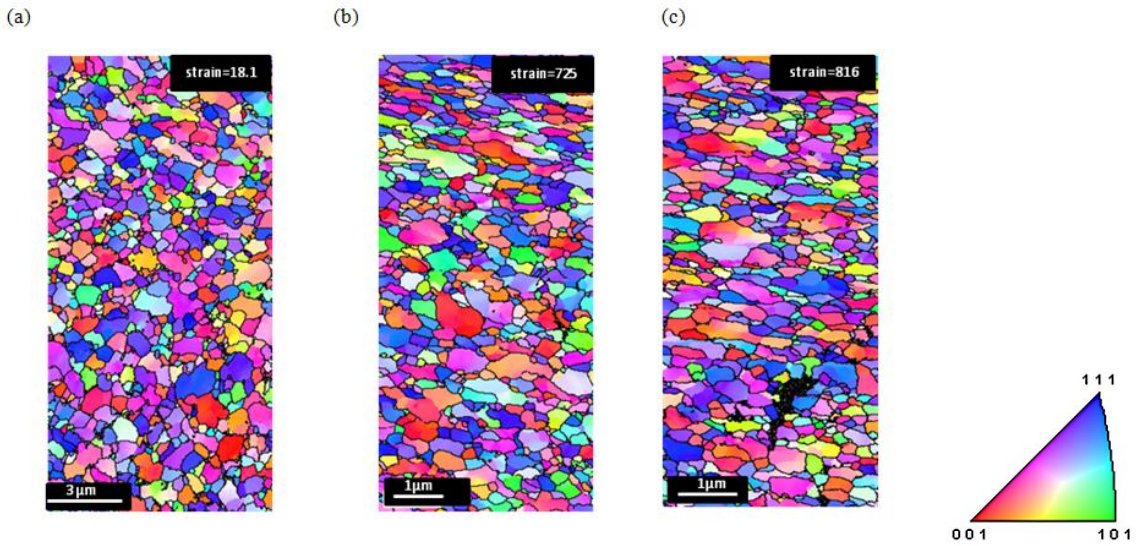

Figure 23: IPF maps showing various locations in the CP Cu disk processed up up to 50 turns of HPT: The average radial distance of each location was (a) ~0.1, (b) 4 and (c) 4.5 mm from the center. The corresponding average strain value is shown in the top-right corner of each IPF map.

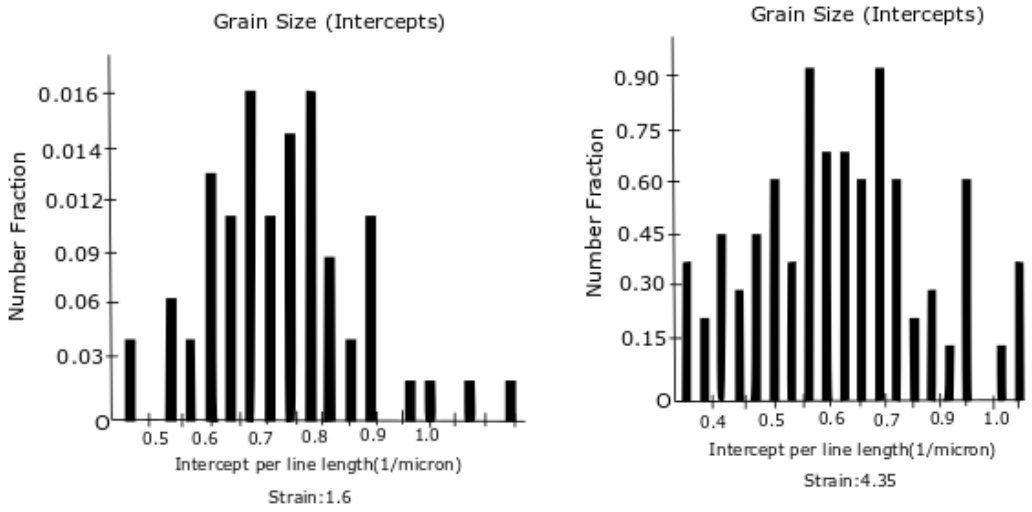

Figure 24: Histograms showing the grain distribution in as-fabricated sample processed up to a strain of (a) 1.6 and (b) 4.35 strains in the disk processed to ½ turn.

Figure 25 summarizes the EBSD data by plotting the variations of grain size (d), length per unit area of the low angle grain boundaries (l_{LAGB}) and the high angle grain boundaries (l_{HAGB}), and length per unit area of the total grain boundaries (l_{TGB}) as a function of the equivalent strain imposed during HPT processing for both the as-fabricated and naturally aged samples to study the effect of natural ageing on the HPT processed samples. All the boundaries in these plots were quantified as total boundary length per unit area

because EBSD scans were taken over different scan areas and hence it is required to desensitize the numbers relative to the scan area for the proper comparison.

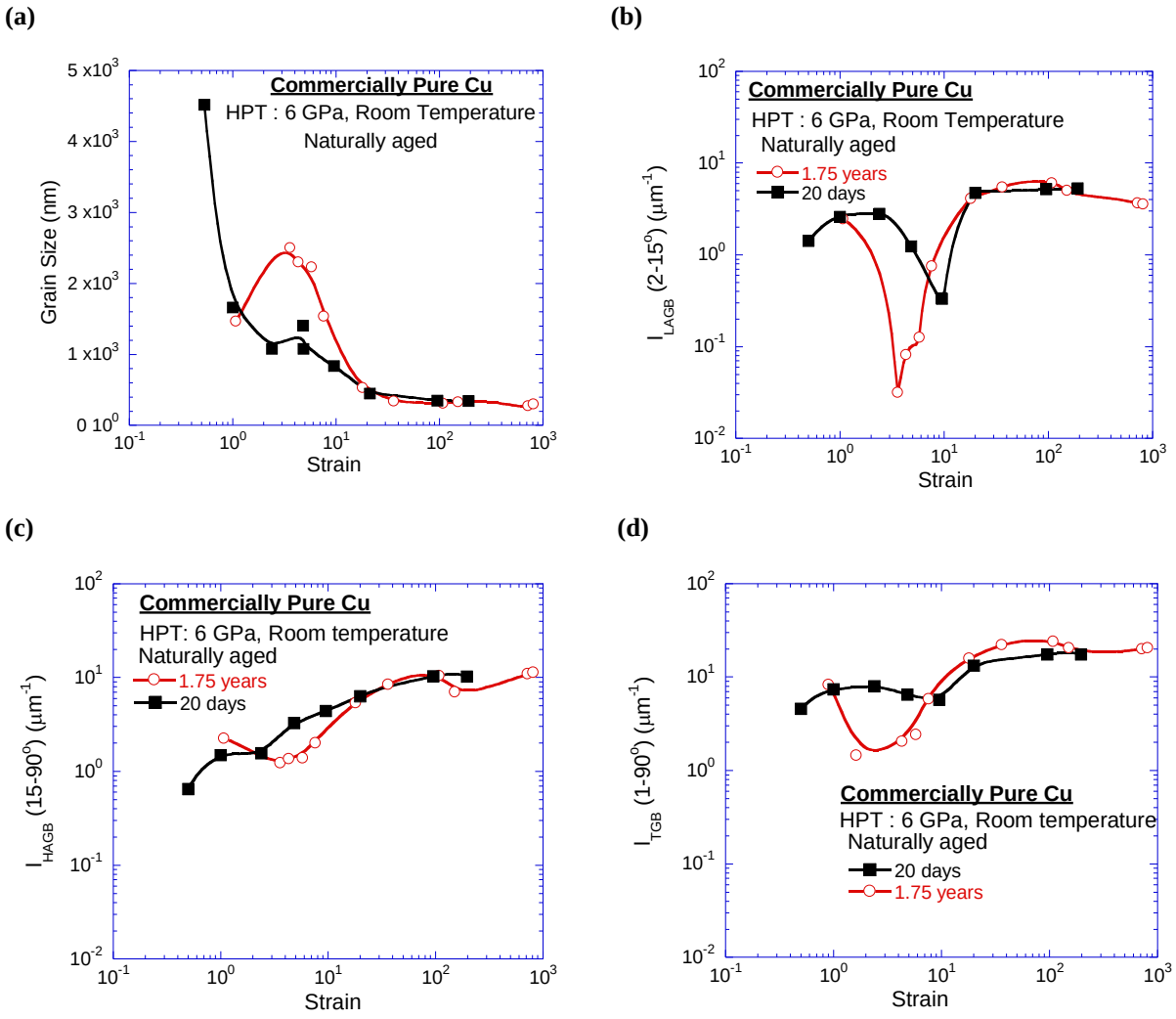

Figure 25: Variation of (a) grain size (d), and length per unit area of the (b) low angle boundaries (l_{LAGB}), (c) high angle boundaries (l_{HAGB}), and (d) total grain boundaries (l_{TGB}) as a function of strain imposed during HPT processing for both naturally aged sample as well as as-fabricated sample. Here, the data for coarse-grained CP Cu is not shown.

As shown in **Figure 25a**, for the as-fabricated sample, grain size was approximately 4.5 μm at the strain value of 0.5, and then its value gradually decreased and saturated at the value of 350 nm. However, the trend is different for the naturally aged sample: the refined grain size of 1.5 μm increased slightly to 2.5 μm at the onset of HPT straining and rapidly decreased to a saturated value of ~300 nm after the HPT strain of ~40. This is consistent with other studies showing the grain sizes of a few hundred nanometers in Cu by HPT processing [20, 21]. Nevertheless, the data shown in **Fig. 25a** clearly shows that there was grain growth

in the lower strain region of 2 to 10 due to the prolonged natural ageing. However, there was no significant change in the grain size in the higher strain regions due to natural ageing.

Figure 25b shows the variation of the length of the low angle boundaries, for the as-fabricated sample: the value of l_{LAGB} decreased monotonically up to a strain of 10 and thereafter it increased to saturate with the HPT processing. However, for the naturally aged sample, the value of l_{LAGB} decreased gradually up to a strain of 3 and remained low up to strain of 5, and then it increased to saturate with the HPT processing. **Fig. 25b** reveals that although the trend of the variation of l_{LAGB} was the same for both conditions, there was a significant variation in the low strain region (i.e., between ε_{ev} of 2-10), where a decrement in the value of length of the low angle boundaries was observed after naturally ageing. The drop of l_{LAGB} at the strain of <10 can be attributed to the formation of sub-grains due to the plastic deformation, which then transformed into grains with high angle grain boundaries upon continued plastic deformation by HPT. Furthermore, a comparison of **Figures 25b** and **25c** reveals that even after l_{LAGB} saturated to its upper limit, the overall length of the high angle grain boundaries was more than the low angle grain boundaries, and the difference tends to be apparent with increasing numbers of HPT turns through 10 to 50 turns. Hence, as shown in **Figure 25d**, the variation of l_{TGB} followed the trend of l_{HAGB}. The trend of variation of length of high angle boundary and total boundary are similar for both as-fabricated sample and naturally aged sample except in the small strain regions (i.e., ε_{ev} of 2-10).

The interesting fact is that all noticeable variations due to the natural ageing, i.e., increment in the grain size, and decrements in l_{LAGB}, l_{HAGB} and l_{TGB} , were observed to occur in the low strain region of 2-10. Hence, it indicates that there was grain growth in this strain regime. The grain growth might occur due to accumulation of the strain, and more heterogeneity in the microstructure, which is likely to occur more at relatively small strains, must have made the sample more susceptible for nucleation and growth of the recrystallized grains during ambient aging. Another possibility might be that the grain growth occurred without recrystallization. To identify the dominant mechanism responsible for observed grain growth, further microstructural examination, wherein the evolution of orientations of particular sets of grains during natural ageing is recorded, is required.

It should be noted that the hardness profile of the samples processed by HPT for 10 and 50 turns followed by ambient aging did not show any abrupt variation in both the microstructure and hence the hardness value, which were >3 times higher than the annealed coarse-grained sample without HPT. This retention of the exceptionally high hardness of CP

Cu over long periods confirms the potential of the HPT processed samples to be used in long-term applications.

4.2.3 Hardness: Structure-property relationship

The higher hardness value in a material is often attributed to the smaller grain size. The anomalous behavior of the ½ turn sample after naturally ageing is caused due to grain growth in the particular strain regime between 2 to 10. If the hardness value of the ½ turn sample is observed, the grain size in the central region was the smallest leading to the highest hardness in the sample as per the Hall-Petch relationship. On the contrary, the grains near the disk periphery were only marginally (~4.8 %) larger than the grains in the central regions; however, the hardness at the peripheral region was substantially lower than that of the central region of ½ turn disks. This anomalous deviation from Hall-Petch relation may be attributed to the high value of the low angle grain boundaries in the central region of the sample. Hence, although grain size is an important contributor to the strengthening of CP Cu, the role of low angle boundaries is critical in determining the overall strength of the sample. This is further elaborated next in light of Hall-Petch relationship.

Figure 26 shows the variation of hardness of the HPT processed CP Cu samples as a function of the inverse of the square root of grain size, *d*, under both the as-fabricated and naturally aged conditions. It shows a linear variation between the hardness and $d^{-0.5}$, which is delineated by a dark dashed line, for most of the datum points and the result reveals the validity of the Hall-Petch relationship for the HPT-processed CP Cu samples after natural ageing. The main outlier, which is shown by an arrow in **Figure 26a**, was obtained from the central region of the disk processed for ½ turn by HPT. As discussed earlier, the grains in the central region of the sample were relatively very small and comprised of significantly large numbers low angle boundaries and twin boundaries as compared to the grains in the regions away from the center. **Figure 26b** shows a similar variation for the fabricated sample, and it is observed that a few data points deviate from the Hall-Petch regime (shown by the crossed rectangular box). Further analysis shows that all the deviated data points have a large number of l_{LAGB} in both as fabricated as well as naturally aged conditions. Hence, it indicates that the strengthening due to low angle boundaries, which is not explicitly accounted in Hall-Petch relationship, also plays a critical role during initial straining, where larger fraction of low angle boundaries are formed. To examine this hypothesis and hence quantify the effect of low angle boundaries, grain were redefined by a misorientation of more than 1^{o}, a new plot showing variation of Vickers hardness as function of the inverse of the square root of the

modified grain size was prepared[4]. As shown in **Figure 26c**, majority of the data point that were outliers when standard definition of grain was used fell more closely into the Hall-Petch regime. Hence, it can be concluded that the effect of low angle boundary strengthening should be considered for establishing the Hall-Petch relationship for the HPT processed sample.

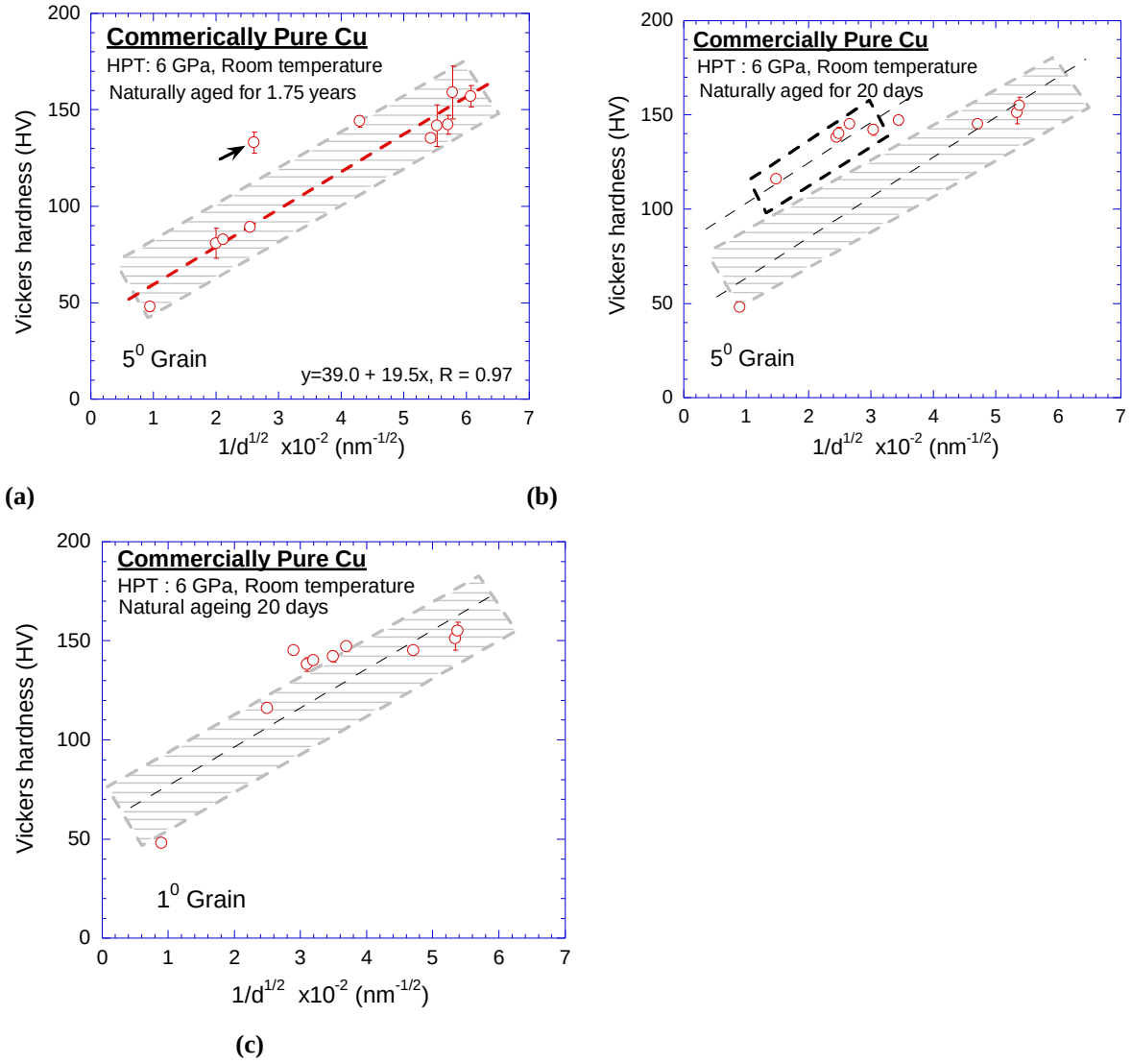

Figure 26: Effect of HPT processing on the hardness of commercially pure Cu: Variation of Vickers microhardness of as function of the inverse of the square root of grain size for (a) naturally aged sample considering 5° misorientation, (b) the as-fabricated sample considering 5° misorientation and (c) the as-fabricated sample considering 1° misorientation for defining a grain.

Another possible reason for the deviation from Hall-Petch relationship could be the difficulty in calculating the effective grain size, i.e., the representative value of the grain size given the heterogeneity in the microstructure (see **Figure 20**): As mentioned earlier, average grain size was calculated in this study for all regions (irrespective of Gauss distribution was

[4] The default definition for the grains in this study was a misorientation of more than 5°.

observed or not) and due to more heterogeneity in grain size distribution, especially in the low strain regime, the calculated grain size might not be truly representative of the effective grain size in context of mechanical strength. In other words, it remains unclear how one should estimate an effective grain size, which can then be used in standard Hall-Petch relationship, for a material where there is a colony of large number of small grains next to a colony of a fewer large grains, as observed in the samples after low number of HPT turns (see **Figure 19**).

4.3 Effect of residual stress on hardness value

The residual stress in the HPT processed-naturally aged Cu samples was evaluated by calculating the shift, relative to the unstrained annealed condition, in the position of the 2θ-peak corresponding to (111) plane using **Equation 3**. This shift in the peak position was calculated relative to the reference peak for the annealed Cu samples where the annealed sample is considered to have no residual stress. **Figure 27a** shows a representative I-2θ plot showing a shift in the peak position for a Cu sample with an HPT strain of 22 relatives to the peak of the annealed Cu. A rightward shift in the peak position of (111) plane was readily discernible in **Figure. 27a**, which indicates a decrease in the interplanar spacing and hence it corresponds to compressive residual stress. Although it appears reasonable, given the large compressive stress applied during HPT processing, it also indicates that there would be a tension-compression asymmetry in the mechanical properties of HPT processed-naturally aged Cu (e.g., the difference in yield strength, etc.); this should be investigated further. Furthermore, as mentioned before, a fraction of the section will also be under tensile residual stress to maintain the force balance and hence the evaluation of tension-compression asymmetry in HPT processed sample should be performed carefully.

Figure 27b shows the variation of the estimated residual stresses in the top layer of the HPT processed and naturally aged Cu samples. It should be noted that the strain shown on the abscissa in this graph corresponds to the mean of the shear strains across the sample investigated and the corresponding residual stress value shown on the ordinate is the average of three sets of readings obtained from the sample by mounting it on the sample holder at three different occasions. Since variation in the location of the top surface of the sample with respect to the source-detector position can result in a shift in the peak position, the above adopted method was applied to minimize the effect of positioning of the sample onto the sample-stage on the XRD measurements. In addition, a consistency between the top surface of the sample and the prescribed position of the sample for analysis was ensured by calibrating

height adjustment each time before taking readings. As revealed by small error bars associated with all readings, positioning of the sample in the x-ray diffractometer was repeatable and hence it is expected to be at the prescribed position. It can be observed from **Figure 27b** that the residual stress in all the HPT samples varied a little with strain and can be inferred to be within a band of 72 ± 5 MPa (in compression), which was attained just after a shear strain of 4. Yield stress, σ_{ys}, was calculated from the Vickers microhardness value using the relation, $\sigma_{ys} \approx (1/3)\, H_{HV}$, where H_{HV} is the Vickers microhardness value calculated in units of Pa [44].

(a) **(b)**

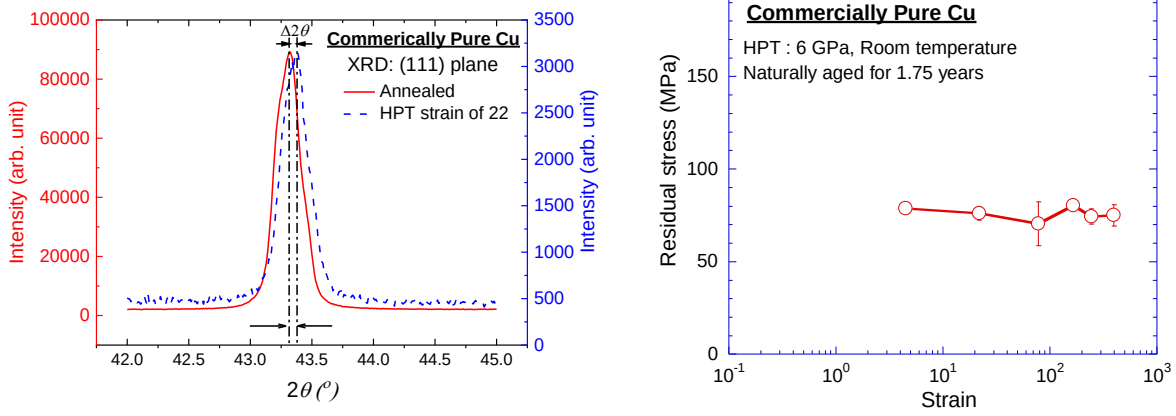

Figure 27: (a) An example plot showing the shift in the peak position obtained in XRD pattern due to the presence of residual stresses, and (b) variation of the residual stresses near the surface of the sample (up to a depth of 4.46 μm) with HPT strain in the samples processed through HPT followed by natural ageing for 1.75 years.

Figure 28 shows a comparative plot of yield stresses and the residual stresses for the sample processed by HPT followed by prolonged natural aging. It can be observed that the residual stresses generated by HPT processing did not have any significant effect on the hardness or yield stress values at high strains. Thus, the exceptionally high value of hardness at higher strains (including at a strain of less than 2, wherein it shows a high hardness value before the onset of the dip in the value – see **Figure 28**) is not solely due to the residual stresses present in the sample.

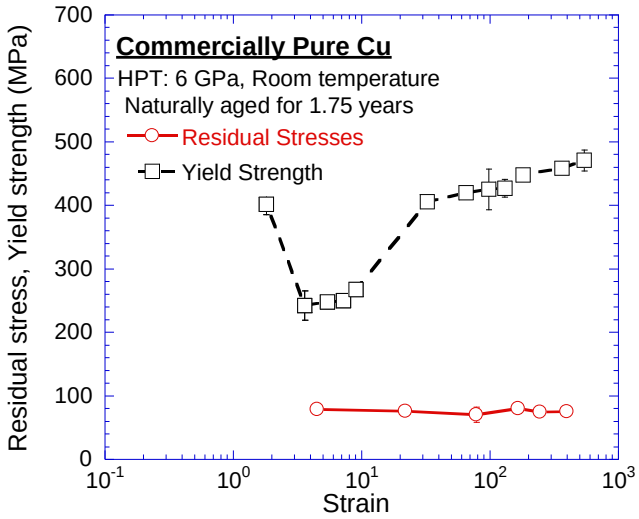

Figure 28**:** Variation of the yield strength of material (as calculated from Vickers microhardness data) and the residual stress as a function of HPT strain.

4.4 Effect of HPT on electrical resistivity

Electrical resistivity was measured using the customized measurement setup described in Chapter 2. The tests were performed on the miniaturized samples having dimensions approximately 1.5 × 1.0 × 0.55 mm^3 for both the as-fabricated samples and naturally aged samples. **Figure 29** shows the variation of electrical resistivity as a function of equivalent strain for both types of CP Cu samples. The material in the annealed condition, i.e., without HPT processing, showed an electrical resistivity of 17.3 nΩ-m, as shown by the left-most point in **Figure 29** (since it is a semi-log graph where zero cannot be plotted on x-axis, a small value of strain corresponding to 0.1 was prescribed to this condition). The variation of resistivity follows the similar trend for both types of samples: the electrical resistivity of the CP Cu increased gradually to 21.0 nΩ-m after a small strain of ~7, followed by a drop to a value of 17.6 nΩ-m. This drop was followed by a gradual increase in the resistance to a value of ~22.0 nΩ-m for a strain of ~400. These changes are more than the error bar associated with these measurements and hence the effect of HPT processing shows the non-monotonous fluctuation of electrical resistivity and it is observed that there is no significant effect of natural ageing on the electrical resistivity value of the CP Cu processed by HPT.

The variation and overall values of electrical resistivity obtained in this study are similar to that reported on high purity Cu by Edalati *et al.* [20], where they performed HPT processing at 2 GPa and measured average resistivity of 4 mm long sample as compared to ~ 1 mm long sample in this study. However, the electrical resistivity of CP Cu was only marginally affected by the HPT processing (e.g., within ± 10 % over a strain of 900 – see

Figure 5). Hence, the effects of HPT pressure, purity of Cu and microstructural inhomogeneity do not affect the electrical resistivity of HPT processed Cu. On the other hand, Zhilyaev *et al.* [22] observed maximum value of ~27.0 nΩ-m for the electrical resistivity of the HPT-consolidated machined chips of CP Cu at 6 GPa for 5 turns, which is significantly higher than the resistivity values obtained in this study. Moreover, Zhilyaev *et al.* [21] also reported a high value of electrical resistivity of ~25.0 nΩ-m for CP Cu samples processed at 6 GPa to 5 turns of HPT.

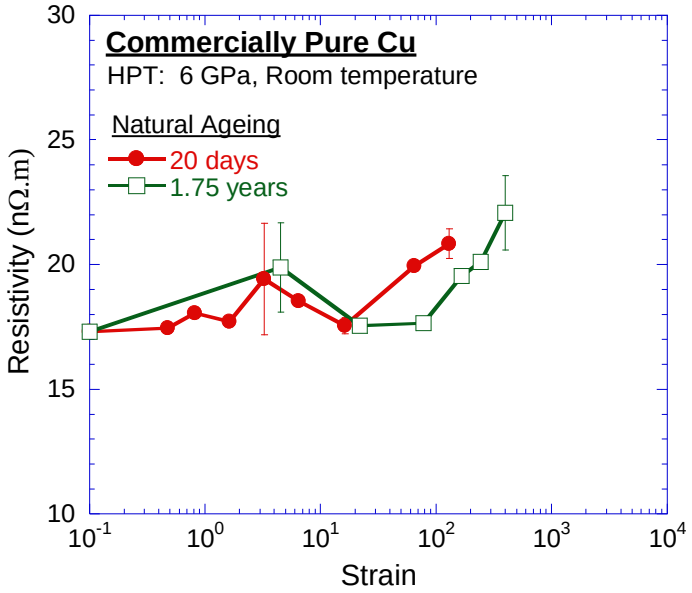

Figure 29: Variation of the electrical resistivity of HPT processed CP Cu as function of the strain imposed during HPT.

Electrical resistivity in this study was measured using ~1 mm long strips, which captured the effect of HPT strain on the local electrical conductivity more accurately, as compared to the earlier studies using much longer samples. It reveals that HPT processing following by ambient ageing increased the resistivity of CP Cu by only ~20 % at the strains where it enhanced the hardness by ~300 %. The electrical resistivity of the CP Cu samples was significantly smaller than those reported on the HPT processed CP Cu [21, 22] and were in the range of those reported for the HPT processed high purity Cu samples. Such a combination of high conductivity and excellent hardness has never been reported in CP Cu and hence these HPT-processed CP Cu has an excellent potential for the electrical connector applications.

4.4.1 Electrical resistivity: Structure-property relationship

As shown in **Figure 29,** there was no effect of the natural ageing on the electrical resistivity of the HPT processed samples. **Figure 29** shows that the electrical resistivity increased with HPT processing at lower strains and then it decreased with subsequent HPT straining, thereafter, increased again to a relatively larger value at very high strains. The possible obstacles in the path of electrons in a material can be boundaries (such as grain boundaries including low angle, high angle, twin boundaries, etc.), defects (such as dislocations, vacancies, etc.); these can be analyzed to understand the variation of resistivity in CP Cu samples.

Firstly, in order to understand the role of the total length of grain boundaries in the electrical resistivity of the HPT-processed CP Cu, variation of the electrical resistivity was plotted with the total length per unit area of the grain boundaries (see **Figure 30**). It should be noted that since the l_{TGB} was not available at every location or strain at which the electrical resistance values were measured, its value for a given location or strain was interpolated from the two nearest values. As shown in **Figure 30**, the electrical resistivity of the HPT-processed CP Cu samples varied non-monotonically with l_{TGB}, thereby suggesting that grain boundaries did not play a significant role in electron scattering and hence determining the electrical conductivity of these samples. It implies that some other phenomenon, such as electron-phonon scattering as suggested by Zhilyaev *et al.* [21] is responsible for the observed effect of strain imposed by HPT on the electrical conductivity.

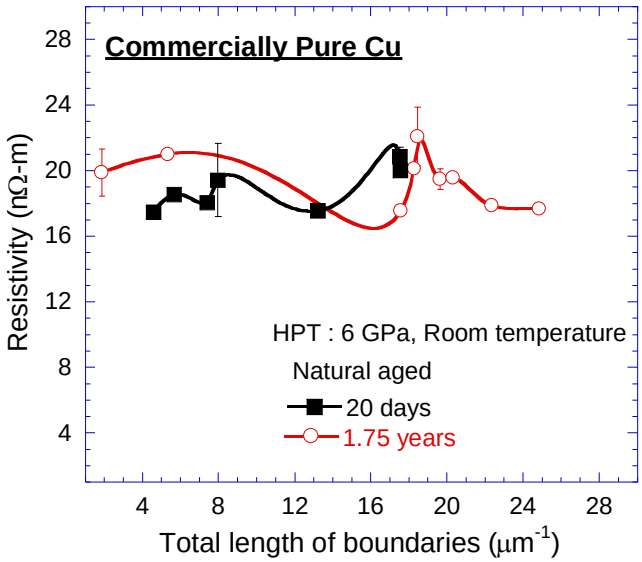

Figure 30**:** Variation of the electrical resistivity of CP-Cu samples processed through HPT followed by ambient-ageing for 1.5 years as well as as-fabricated sample as a function of the total length per unit area of grain boundaries.

On the other hand, if the variation in the residual stress is observed (see **Figure 31**), then it appears that a decrease in the residual stress leads to a decrease in the electrical resistivity at low as well as moderate HPT strains (e.g., up to ~10^2). Since the residual stress suggests a change in the lattice spacing, it would imply a difference in the scattering efficiency of lattice points in the stressed lattice as compared to the unstressed lattice. However, a careful observation of the variations of the electrical resistivity and the residual stress reveals that there was weak to moderate correlation between them. Even though the values of the residual stresses were within the error bar, the average value of the residual stress showed some trend with the variation of the residual stress. Hence, it can be inferred that the residual stress should definitely be considered for understanding the variation of the electrical resistivity in Cu due to HPT straining; however, it may not be solely responsible for the observed variation. It is inferred that defect concentration, such as dislocation density and vacancy concentration, should also be considered and further explored to truly understand the dominant route through which HPT straining affects the electrical resistivity of commercially pure Cu.

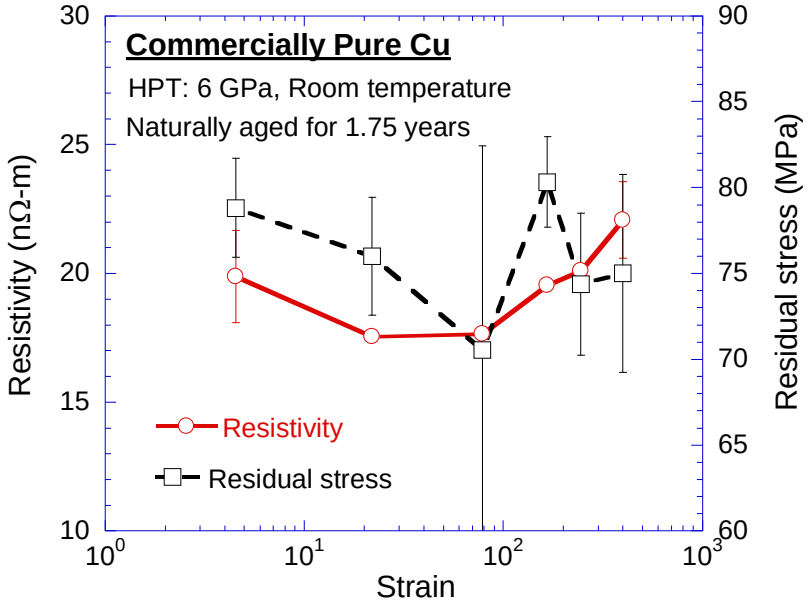

Figure 31: Variation of electrical resistivity as well as the residual stress as function of strain.

4.5 Effect of HPT on fatigue behavior of CP Cu

4.5.1 Formation of surface micro-cracks

Fatigue tests in bending were performed by applying different maximum stresses, which were calculated by using the linear elastic theory and the maximum displacement of free end, which was measured using a laser beam. **Figure 32** shows the optical images

showing the micro-crack on the surface of the Cu sample processed up to 50 turns of HPT (and with less than 2 months of natural ageing). Tests were performed at maximum stress values of 170, 185 and 200 MPa. It can be observed from **Figure 32** that the density of the surface micro-cracks in all tested samples was more near the fixed end (i.e., in the region of the highest stress). Further **Figure 32** also reveals that if the maximum stress in the cantilever type of these samples was increased from 170 to 185 MPa, then the region of micro-cracks spread over larger region away from the fixed end, and the same trend continued, rather more drastically, upon increasing the stress further to 200 MPa. Hence, it shows that, as expected, the density of the surface crack depended strongly on the stress in the particular region.

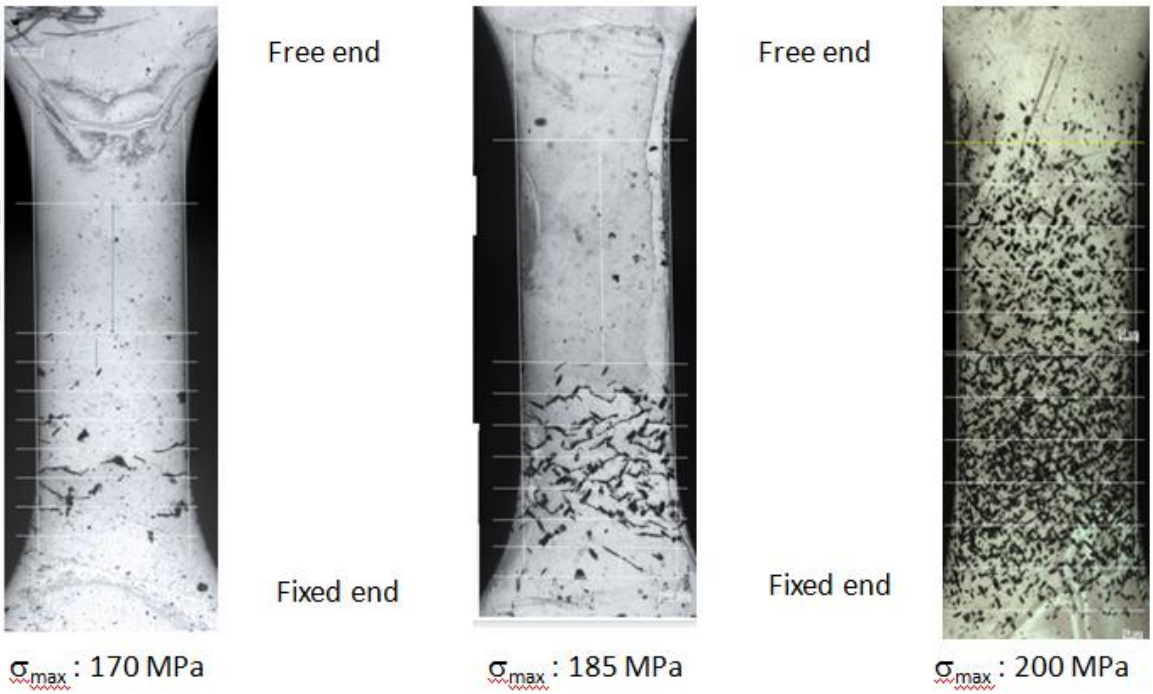

(a) **(b)** **(c)**

Figure 32: Optical micrographs showing the micro-cracks formed on the surface of the fatigued Cu samples that were processed up to 50 turns of HPT and tested within 2 months of natural ageing: Maximum stress near the fixed end of (a) 170, (b) 185, and (c) 200 MPa. The fixed end was near the bottom of each micrograph.

Figure 33 shows the optical micrographs of the annealed samples fatigue-loaded at the maximum stresses of 80 and 172 MPa. Since the surface cracks were not clearly visible in the optical images, micrographs at higher magnifications were obtained using an SEM. To maintain consistency, 50 turns HPT samples were also examined using SEM after fatigue testing. **Figure 34** shows a few representative SEM micrographs of the fatigued annealed samples that were tested at maximum stresses of 80 and 172 MPa. The micro-cracks were

unambiguously visible in the SEM micrographs, and some deep long microcracks in the sample tested with a maximum stress of 172 MPa were readily discernable (see **Figure 34b**). On the other hand, **Figure 35** shows a few representative SEM micrographs, taken at different magnifications, of the HPT fatigued samples: While similar to the annealed samples, micro-cracks in the HPT processed samples were also significantly clearer in SEM micrographs, the number density of micro-cracks, especially finer cracks, were significantly higher in the HPT processed sample.

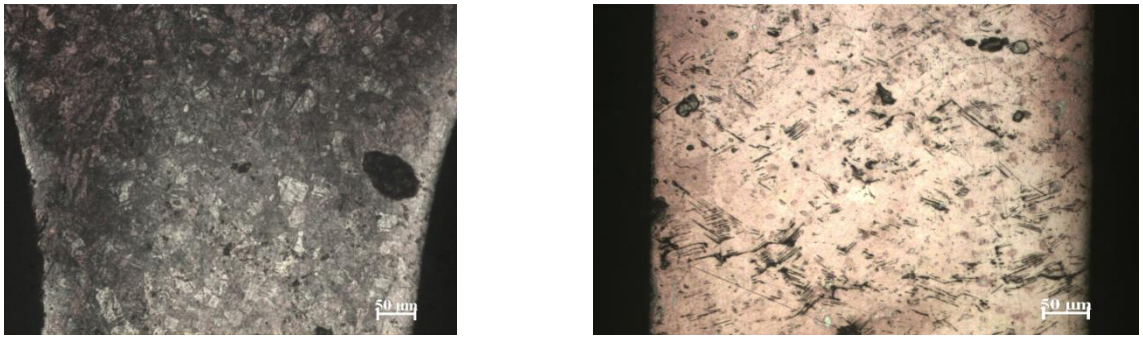

(a) **(b)**

Figure 33: Optical micrographs showing micro-cracks on surface of the annealed Cu samples after fatigue loading at the maximum stress of (a) 80 and (b) 172 MPa.

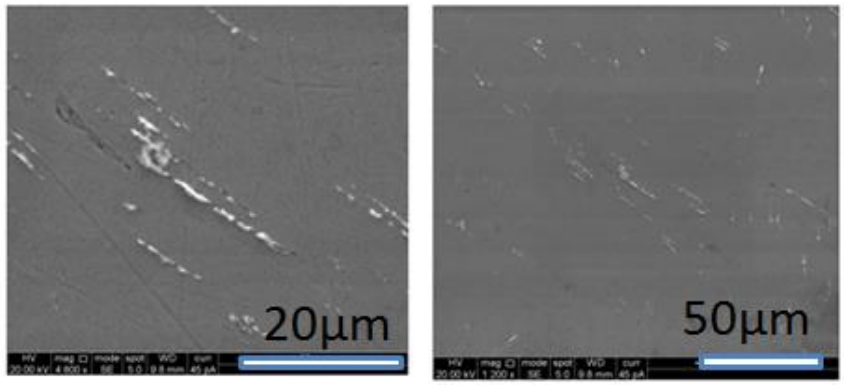

(a)

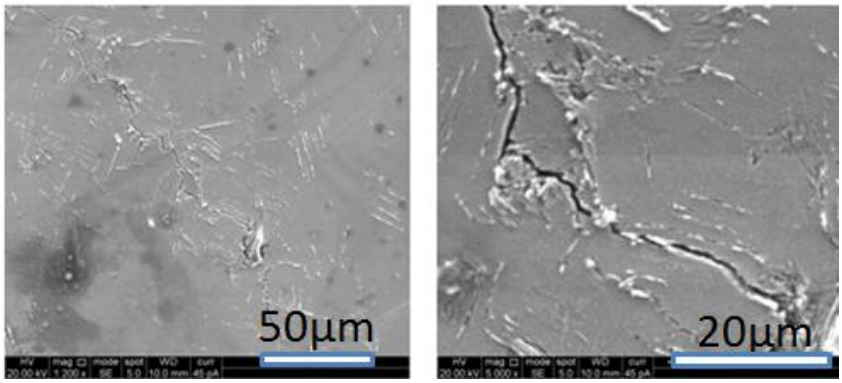

(b)

Figure 34: SEM micrographs showing micro-cracks on surface of the annealed Cu samples after fatigue loading at the maximum stress of (a) 80 and (b) 172 MPa.

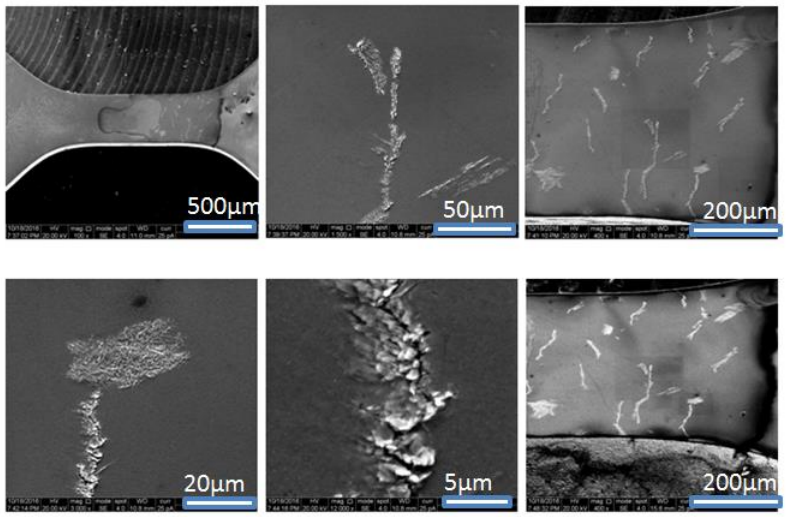

(a)

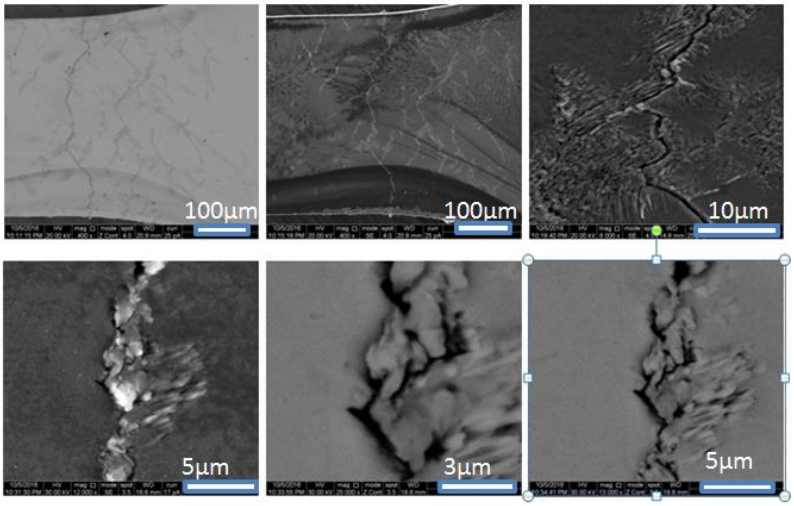

(b)

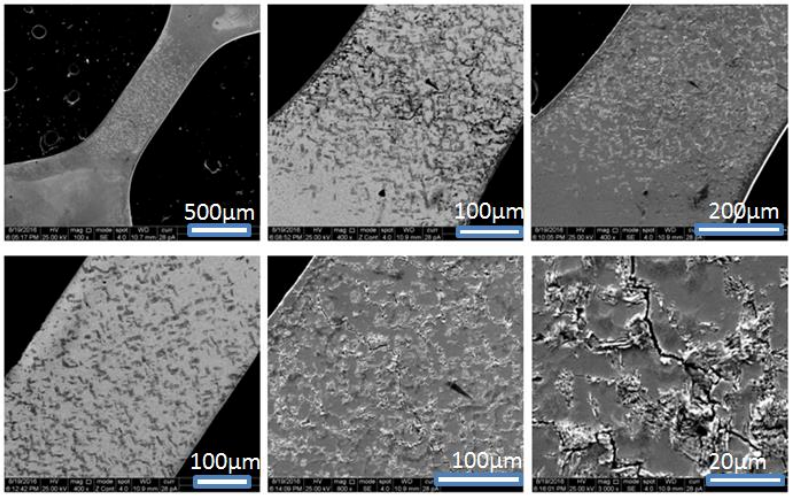

(c)

Figure 35: SEM images showing the surface crack on the fatigued Cu sample processed by HPT up to 50 turns (a) maximum stress value of 170 MPa (b) maximum stress value of 185 MPa (c) maximum stress value of 200 MPa.

4.5.2 Dependence of surface crack density on stress

Area fraction of the region with surface crack was measured using Image-J image analysis software. Small rectangular boxes were drawn over an optical image, as shown in the **Figure 36**, and by applying the threshold contrast in the Image-J software, the area fraction of the surface crack in each section of the sample was calculated. Stress was estimated by using the basic bending equation for linear elastic condition, given as follows:

$$\frac{M}{I} = \frac{\sigma}{y}$$

where M is the moment, I is the moment of inertia (equal to $bh^3/12$, where b is the width and h is the height of the sample with rectangular cross-section), y is vertical distance away from neutral axis and σ is the normal or bending stress along the length of the sample. The above equation will be validated using finite element analysis, as discussed in **Appendix I**.

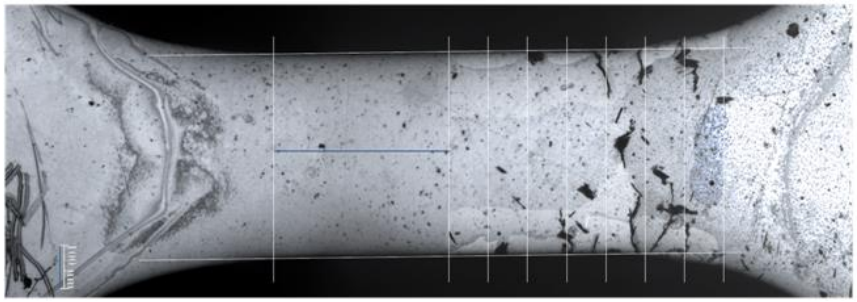

Figure 36: Optical images showing rectangular boxes drawn on an image of the sample for calculating the area fraction of the surface micro-cracks using Image-J image analysis software.

Figure 37 shows that the area fraction of the regions with the surface micro-crack increased with the stress at the given location. Now, if the area fraction of the surface cracks would have been only the function of the stress at a location, then for the same value of stress there should have been the same area fraction of the surface micro-cracks. This is generally true for most of the stresses; however, **Figure 37** shows a notable exception: area fraction of the micro-crack comprising regions loaded to lower stresses in the sample with maximum stress of 200 MPa (i.e., the highest stress used in this study) was significantly more. Hence, it appears that the spread of the regions comprising micro-cracks also depended on the value of the maximum stress in the sample.

This observation is quite intriguing as the grain sizes in these samples were very small (~300 nm) and hence the probability of dislocation activity in a grain getting affected by further away grains witnessing high stresses should be very low. Furthermore, yield strength of 50 turns HPT sample was ~500 MPa (based on hardness value) and hence the stresses in

this “cantilever” sample during fatigue was well below its yield strength. It is speculated that formation of large number of “breathing cracks” in these cantilever type fatigue samples can lead to a non-linear change in the frequency profile of the sample. This is particularly true when the high stress regions became heavily populated with micro-cracks (e.g., in 200 MPa sample). Now, with increase in the surface cracks, the compliance of the system would non-linearly increase. This would generally lead to a decrease in the resonant frequency (as consistently observed in this study) and, more importantly, the maximum displacement of the piezo-drive must decrease to obtain the same stress profile (so that the stress concentration is accounted for). However, the stress calculation shown here was based on the crack-free condition and the displacement was actively not controlled to maintain the stress profile in presence of micro-cracks (which are affecting the resonant frequency in non-linear fashion). This would then lead to an increase in the effective stress at a location, which will be quite significant if the stress values are very high. In other words, the regions of the samples affected by micro-cracks should be shifted rightwards on the stress axis to account for the effective stress acting in that region. Nevertheless, one may reasonably conclude that the area fraction of surface micro-cracks increased with an increase in the stress amplitude.

(a) (b)

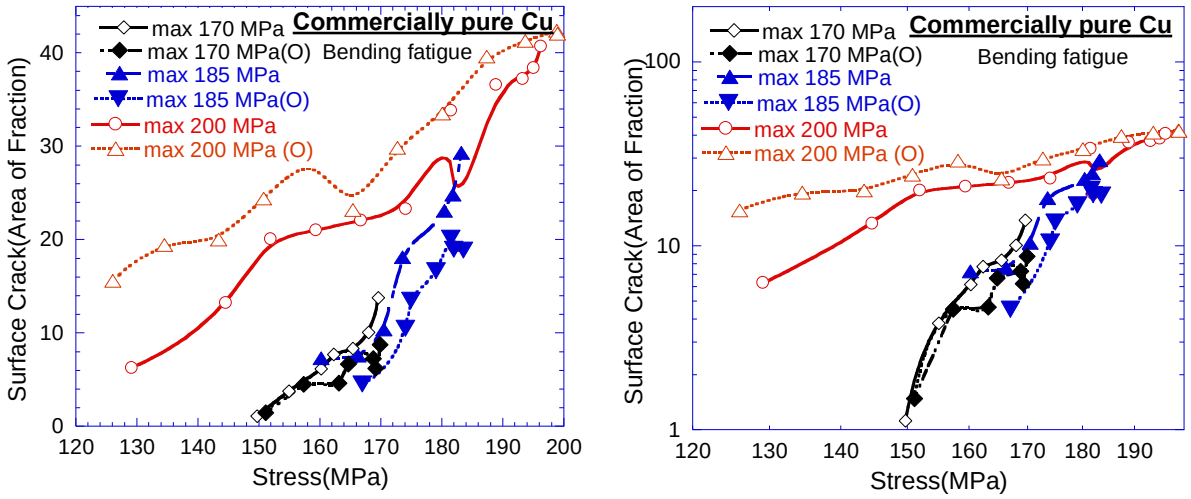

Figure 37: Variation of area fraction of surface cracks after fatigue testing of HPT processed samples as a function of the stress: (a) linear axes and (b) log axes. Here, the letter (O) represents the flipped side of the sample.

Figure 38 shows the variation of the area of a fraction of surface crack with respect to stress value for both annealed and HPT processed samples after fatigue testing. **Figure 37** readily reveals that the area of surface cracks was very small in the annealed sample. However, although its value was small, surface crack formed in annealed samples even at low-stress value. On the other hand, the surface cracks did not readily form in the low-stress regime in the HPT processed samples; however, they were quite frequent when the stress became more than a certain value. It indicates that HPT processed sample suppressed the crack nucleation effectively only in the low-stress regions during the fatigue.

(a) (b)

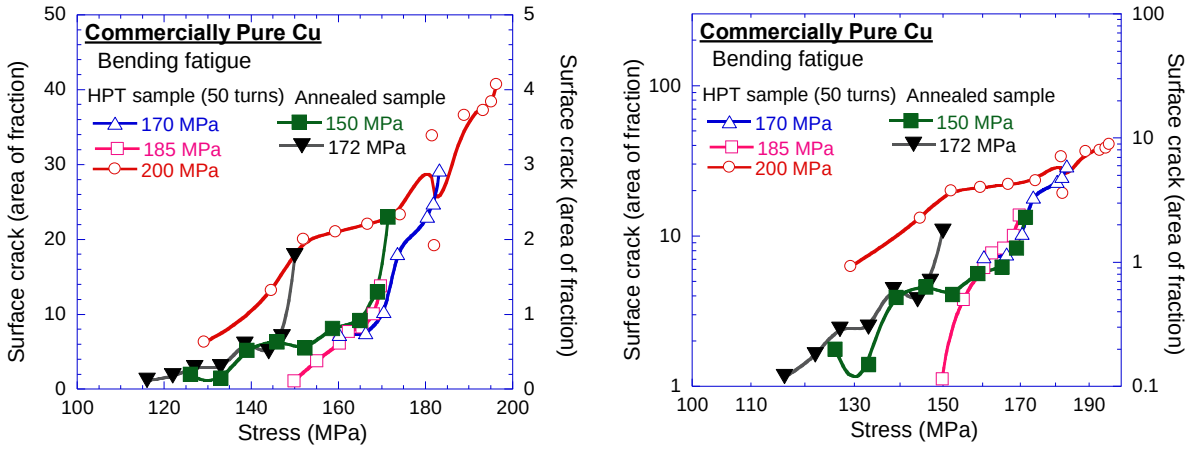

Figure 38: Variation of area fraction of surface cracks after fatigue testing of annealed and HPT processed samples as a function of the stress: (a) linear-linear and (b) log-log axes.

To further substantiate the idea of observation of cracks in annealed samples even at low stresses, SEM micrographs obtained from low stress region (i.e., closer to center of the sample) and high stress region (i.e., in vicinity of the fixed end) of both annealed and HPT processed samples are shown in **Figure 39. Figure 39a** clearly reveals observation of micro-cracks even in the low-stress region. It should be noted that for a maximum stress of 80 MPa, the central region of the sample might have been witnessing a stress of only 40-50 MPa and still it showed micro-cracking. On the other hand, **Figure 39b**, which shows SEM micrographs of HPT processed samples, does not show formation of microcracks in the low stress regimes, even though the low stress regions shown here witnessed stress of as high as 80 and 85 MPa.

Hence, the discussions based on **Figures 32-39**, the following two conclusions about effect of HPT processing on surface micro-crack formation can be made: (a) HPT processing is suitable for avoiding cracking at low stresses, and (b) HPT processing leads to formation of

significantly large number of micro-cracks at higher stresses. These two apparently opposing effects can be explained based on the grain-refining effect of the HPT on microstructure of the sample. Since all tests were terminated when a fixed drop in the resonant frequency was observed, one may speculate similar drop of the effective stiffness of the sample when the tests were terminated. In other words, the effect of the surface micro-cracks on reducing the effective stiffness of all samples, irrespective of grain sizes, must be same. Since a fewer micro-cracks were observed in the annealed samples, these micro-cracks must have been much deeper than those observed in the HPT processed UFG CP Cu (See **Figure 40** for a schematic illustration). In other words, the micro-cracks in the HPT processed samples must have been confined to near the surface region: This appears reasonable as penetrating deeper through several high angle misoriented grains is generally considered less favorable for the fatigue micro-cracks, whose growth is plasticity controlled. For these micro-cracks, grain boundaries act as an efficient barrier (see **Figure 40** for a schematic illustration). Due to their inability to grow deeper in UFG material, a larger number of surface cracks must be formed to lead to same change in the compliance. It should be noted that it took more than 1 order of more number of cycles to reduce the stiffness of the HPT processed samples, as compared to the annealed sample. Overall, it can be concluded that damages in the HPT processed samples were not only limited to the surface, but also it took longer to generate equivalent amount of damages in the HPT processed samples. Hence, HPT processing leads to an enhancement in the high cycle fatigue life of a material, which is consistent with several studies based on S-N curve [30, 31, 48-51].

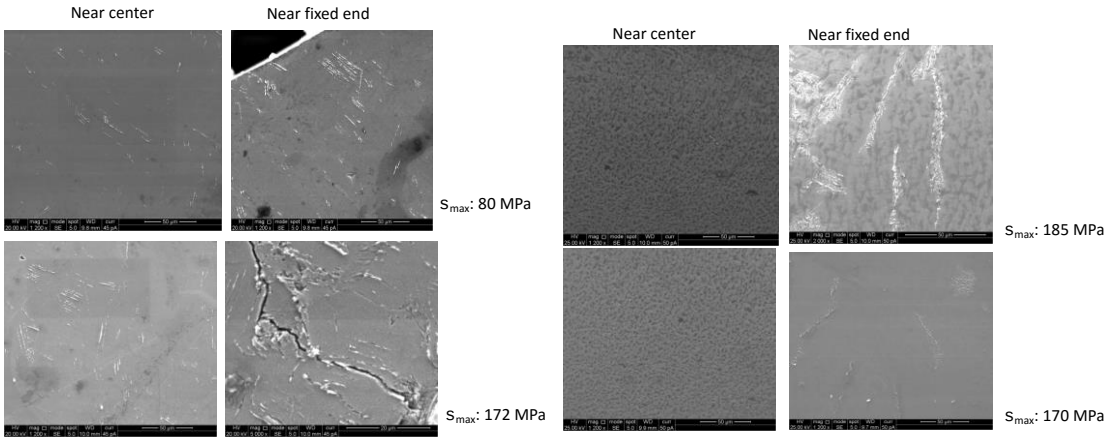

Figure 39: SEM micrographs showing damage accumulation samples after fatigue tests: (a) Annealed sample and (b) sample processed to 50 turns of HPT. As an approximation, the central region can be assumed to have experienced half of the maximum stress applied on the sample.

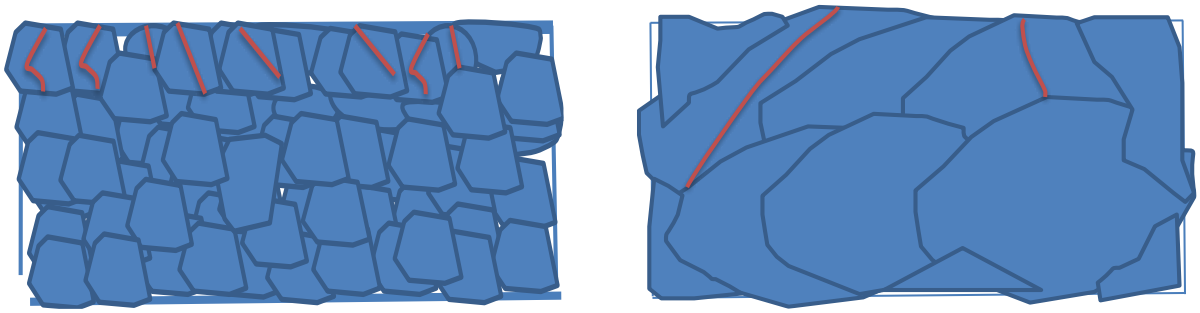

(a) **(b)**

Figure 40: Schematic illustration of growth of micro-cracks under fatigue loading: (a) HPT processed sample comprising ultra-fine grains, and (b) annealed sample comprising coarse grains. In both cases, a grain boundary can effectively stop a fatigue crack from crossing to next grain.

4.5.3 Effect of HPT on dislocation sub-structures formed due to fatigue

Microstructural characterization of the surface cracks showed some intriguing differences between the annealed and the HPT processed samples. To gain further insights into the dislocation substructure, which often reveals the signature of the operational fatigue mechanism, transmission electron microscopy was performed on thin lamella obtained from a region near the surface cracks. 80-90 nm thick lamella were fabricated using the focused ion beam (FIB) machining (see **Figure 41**). TEM imaging was performed using Titan Themis 300 KV system, supplied by FEI (however, it was not aberration corrected) from the FEI. As can be observed from TEM micrograph shown in **Figure 41**, the fabricated lamella was thin enough to achieve electron transparency.

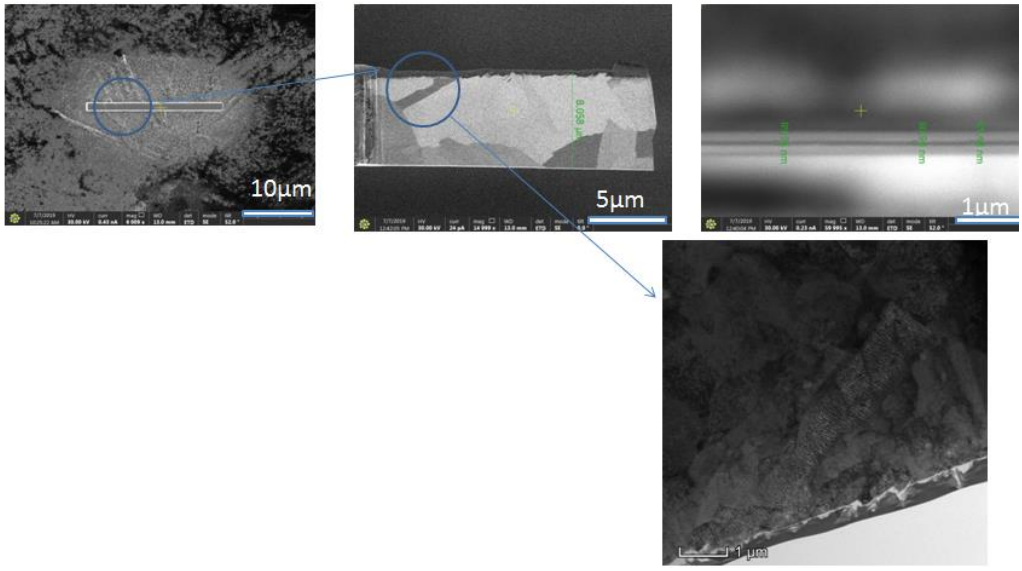

Figure 41: Micrographs showing the lamella prepared using FIB for the TEM analysis. The region of the sample from where the lamella was fabricated is shown by circle in left two micrographs (ion-micrographs). The bottom-right micrograph was obtained using TEM, showing dislocation substructures as well as grain boundaries at low magnification.

Firstly, selected area diffraction patterns were obtained (see **Figure 42a**). Since it is a standard FCC sample (CP Cu), the zone axis (ZA) was kept [101] for obtaining diffraction pattern so that the maneuvering for dislocation imaging could become easier. The sample was then tilted to the particular zone axis to image dislocations. The micrograph shown in **Figure 42b** was taken after tilting the sample along the zone axis with g = $\bar{1}\bar{1}1$ and it clearly shows the dislocations in the annealed sample after fatigue loading. Dislocation were stacked parallel to each other inside the large grains of the annealed sample. Although the dislocation sub-structure may resemble veins and persistent slip bands (PSBs) that often form during fatigue, further analysis, using much higher magnification micrographs, direction analysis, etc., is required to unambiguously conclude it. However, it is reasonable to conclude that the dislocations were arranged parallel to each other due to fatigue.

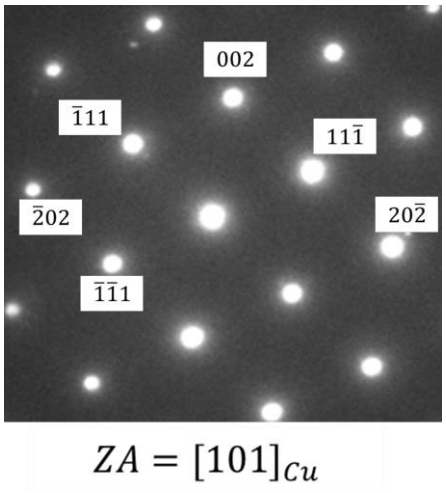

(a)

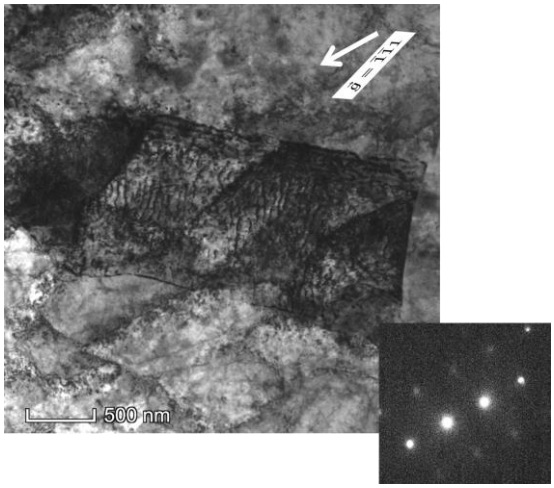

(b)

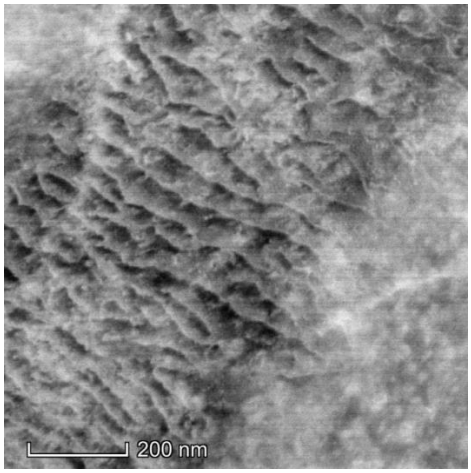

(c)

Figure 42: TEM micrographs obtained from thin lamella of annealed sample following fatigue loading: (a) selected area diffraction (SAED) pattern with [101] zone axis, and (b) low and (c) very high magnification view of dislocations arranged inside a grain. Here, the zone axis, g = $\bar{1}\bar{1}1$ was used to obtain the extinction criterion.

Figure 43 shows the dislocation sub-structure of the HPT processed sample (50 turns) after fatigue testing. Herein also, dislocations were confined within a grain and showed the parallel arrangement. However, unlike annealed sample, the grain size here was significantly smaller, equal to ~ 350 nm, which is in good agreement with the grain size measured using EBSD. This also suggests that the ultra-fine grains produced by HPT of CP Cu remained stable during fatigue loading. Except for the grain size and hence the distance over which the dislocation formation was confined, the dislocation sub-structure formed in annealed and HPT processed samples after fatigue were identical. Since the initial dislocation sub-structures in annealed and HPT processed samples would be very different (e.g., significantly higher dislocation density in HPT processed samples as compared to annealed sample), one may conclude that difference in the number of cycles taken to reach the same dislocation sub-structure after fatigue in both types of samples, and hence the life before losing same amount of stiffness, was determined by the difference in the initial and final substructure and the kinetics of structural evolution. Since fatigue life of CP Cu was enhanced by HPT processing, one may speculate that a the fatigue life of a more complex alloy, such as steel, Ti alloys, etc., where kinetics of structure evolution is much slower than that in CP Cu, can be further enhanced through HPT.

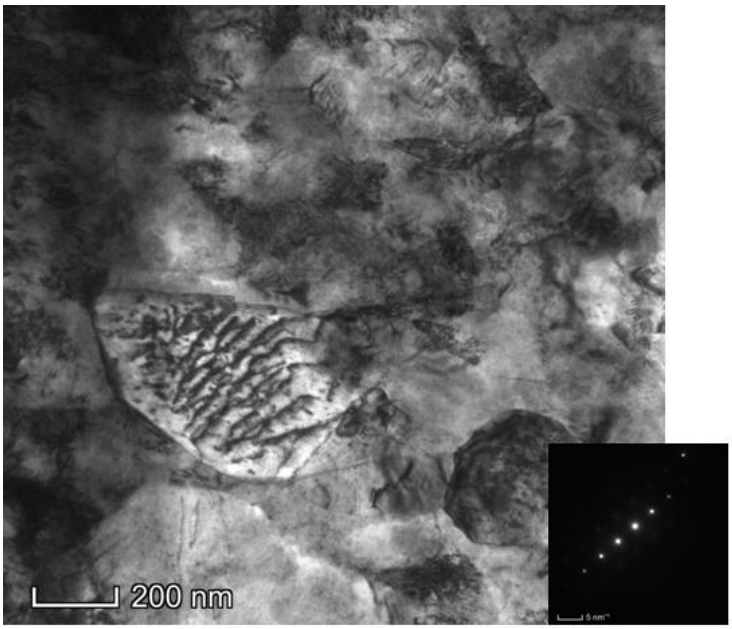

Figure 43: TEM micrograph obtained from thin lamella of HPT processed sample following fatigue loading: A very high magnification view of dislocations arranged inside a grain. Here, the zone axis, g = $\bar{1}\bar{1}1$ was used to obtain the extinction criterion.

5. Conclusion

1. Commercially pure Cu disks were processed by HPT for ¼, ½, 1, 10 and 50 turns at room temperature by applying a compressive pressure of 6 GPa. Some of the HPT processed samples were naturally aged for 1.75 years. Subsequently, hardness, microstructure, electrical resistivity and fatigue behavior of CP Cu were examined to evaluate the processing-structure-property relationship.
2. The hardness value gradually increased with an increase in the HPT strain and got saturated. However, in the case of the naturally aged sample, there was an occurrence of decrement in the hardness value in low strain region (ε_{ev} = 2-10). This decreases in the hardness value was attributed to the grain growth. In the high strain region, hardness got saturated to a very high value (~150 HV) and there was no effect of natural ageing. Hence, with an increase in the homogeneity in the microstructure, grain growth and related decrease in the hardness could be minimized.
3. Residual stress did not appear to affect the hardness; hardness (and hence yield strength) was primarily determined by grain boundaries.
4. The developed customized setup for measuring electrical resistivity was an effective way of measuring the resistivity of miniatured samples. HPT processing led to an increase in the resistivity of Cu; however, the variation of resistivity with strain was non-monotonous. The length of total boundaries and residual stress may not fully explain the variation in the electrical resistivity. Perhaps phonon-electron scattering due to defects (e.g., vacancies agglomeration, dislocations, etc.) are also contributing to it significantly.
5. The area fraction of the surface crack depended on the stress, as well as the maximum stress in the sample (especially when the maximum stress was very high). In HPT samples, surface cracks did not form at lower stresses; however, their numbers were very high at higher stresses. Dislocation sub-structures after fatigue were qualitatively the same for both HPT processed and annealed samples.
6. HPT strain of ~100 or more produced Cu samples with an excellent combination of strength and electrical conductivity: ~30 % increase in resistivity with a 300 % increase in hardness/yield strength. Also, HPT processing led to an increase in the fatigue damage in the sample, especially at low stresses. It appears that HPT processing can provide an excellent set of properties required for Cu conductors and connectors.

6. References

1. R. Z. Valiev, Y. Estrin, Z. Horita, T. G. Langdon, M. J. Zehetbauer, Y. T. Zhu, *JOM* **2000**, *58 (4)*, 33.
2. R. Z. Valiev, Y. Estrin, Z. Horita, T. G. Langdon, M. J. Zehetbauer, Y. T. Zhu, *JOM* **2016**, *68 (4)*, 1216.
3. R. Z. Valiev, Y. Estrin, Z. Horita, T. G. Langdon, M. J. Zehetbauer, Y. T. Zhu, *Mater. Res. Lett.* **2016**, *4*, 1.
4. T. G. Langdon, *Acta Mater* **2013**, *61*, 7035.
5. T. Mungole, N. Nadammal, K. Dawra, P.Kumar, M.Kawasaki, T. G. Langdon. *J. Mater. Sci.* **2013**, 48, 4671.
6. X. Sauvage, G. Wilde, S. V. Divinski, Z. Horita, R. Z. Valiev. *Mater Sci Eng A* **2012**, 540, 1
7. R. Z. Valiev, T. G. Langdon, *Prog. Mater. Sci.* **2006**, *51*, 881.
8. A. P. Zhilyaev, T. G. Langdon, *Prog. Mater. Sci.* **2008**, *53*, 89
9. V. Y. Mehr, A. Rezaeian, M. R. Toroghinejad. *Materials Design* **2015,** 70, 53.
10. H. Hallberg, M. Wallin, M. Ristinmaa, *Mater. Sci.* **2010**, 527, 1126.
11. K. Edalati, Z. Horita. *IOP Conference Series: Materials Science and Engineering*, **2014,** 63, 012099.
12. A. P. Zhilyaev, S. Lee, G. V. Nurislamova, R. Z. Valiev, T. G. Langdon, *Scripta Mater.* **2001**, *44*, 2753.
13. A. P. Zhilyaev, G. V. Nurislamova, B. K. Kim, M. D. Baró, J. A. Szpunar, T. G. Langdon, *Acta Mater* **2003**, *51*, 753.
14. M. Kawasaki, J. Mater. Sci. **2014**, 49, 18.
15. M. Kawasaki, R. B. Figueiredo, Y. Huang, T. G. Langdon, J. Mater. Sci. **2014**, *49*, 6586
16. N. Gao, C. T. Wang, R. J. K. Wood, T. G. Langdon, *J. Mater. Sci.* **2012**, *47*, 4779.
17. K. Edalati, M. Ashida, Z. Horita, T. Matsui, H. Kato, *Wear* **2014**, *310*, 83.
18. E. Aal, M. I. Abd, H. S. Kim, *Mater. Design* **2014**, *53*, 373.
19. J.-K. Han, H.-J. Lee, J.-I. Jang, M. Kawasaki, T. G. Langdon, *Mater. Sci. Engng.* **2017**, *684A*, 318
20. K. Edalati, K. Imamura, T. Kiss, Z. Horita, *Mater. Trans.* **2012**, *53*, 123.
21. A. P. Zhilyaev, I. Shakhova, A. Belyakov, R. Kaibyshev, T. G. Langdon, *J. Mater. Sci.* **2014**, *49*, 2270.

22. A. P. Zhilyaev, I. Shakhova, A. Belyakov, R. Kaibyshev, T. G. Langdon, *Wear* **2013**, *305*, 89.
23. R. K. Islamgaliev, K. M. Nesterov, Y. Champion, R. Z. Valiev, *IOP Conf. Series: Mater. Sci. Engng.* **2014**, *63*, 012118.
24. S. V. Dobatkin, J. Gubicza, D. V. Shangina, N. R. Bochvar, N. Y. Tabachkova, Mater. Lett. **2015**, *153*, 5
25. N. Y. Jin, A. T. Winter. *Acta Metall.* **1984,** 32, 1173.
26. N. Y. Jin. *Phil. Mag. Lett.* **1987,** 56, 23.
27. F. Ackermann, L. P. Kubin, J. Lepinoux, H. Mughrabi. *Acta Metall.* **1984**, 32, 715.
28. L. Buchinger, S. Stanzl, C. Laird. *Phil. Mag. A* **1985**, 50, 275.
29. C. Laird, P. Charsley, H. Mughrabi. *Mater. Sci. Engng.* **1986,** 81, 433.
30. C. D. Liu, M. N. Bassim, D. X. You. *Acta Metall. Mater.* **1994,** 42, 3695.
31. S. R. Agnew, J. R. Weertman. *Mater. Sci. Engng.* **1998,** *A*244, 145.
32. G. Khatibi, J. Horky, B. Weiss, M. J. Zehetbauer. *Int. J. Fatigue* **2010,** 32, 269.
33. C. Xu, Z. Horita, T. G. Langdon. *Acta Mater.* **2007,** 55, 203.
34. K. Edalati, Z. Horita, T. Furuta, S. Kuramoto. *Mater. Sci. Engng.* **2013** *A*559, 506.
35. C. Xu, Z. Horita, T. G. Langdon. *Acta Mater.* **2007,** 55, 203.
36. Y. Huang, S. Sabbaghianrad, A. I. Almazrouee, K. J. Al-Fadhalah, S. N. Alhajeri, T. G. Langdon. *Mater. Sci. Engng.* **2016**, *656A*, 55.
37. A. I. Almazrouee, K. J. Al-Fadhalah, S. N. Alhajeri, Y. Huang, T. G. Langdon, *Adv. Engng. Mater.* **2019**, 21, 1801300.
38. P. Verleysen, F. van den Abeele, J. Degrieck. *IOP Conference Series: Materials Science and Engineering*, **2014,** 63, 012043.
39. R. C. Weast, *CRC Handbook of Chemistry and Physics*, 64th Edition, CRC Press, Boca Raton, **1984**.
40. http://www.substech.com/dokuwiki/doku.php?id=commercially_pure_nickel_270_high_purity_nickel (accessed on 12th May 2019)
41. B. D. Cullity, R. S. Stuart. Elements of X-ray Diffraction. 3rd Ed. New Jersey: Prentice Hall, **2001**.
42. T. Straub, M. F. Berwind, T. Kennerknecht, Y. Lapusta, C. Eberl. *Experimental Mechanics* **2015,** 55, 1285.
43. N. J. Petch, *J. Iron Steel Inst.* **1953**, *174*, 25.

44. J. R. Cahoon, W. H. Broughton, A. R. Kutzak, *Metall. Trans*. **1971**, 2, 1979.
45. Sangid. M. D. *Trans. Inter.Journal of Fatigue* **2013,** 57, 58-72.
46. S. J. Basinski, Z. S. Basinski, A. Howie. *Phil. Mag.* **1969**, 19, 899
47. P. Lukas, M. Klesnil. J. Krejci, *Phys. Stat. Sol.* **1968,** A27, 545
48. A. T. Winter, O. B. Pedersen, K. V. Rasmussen. *Acta Metall.* **1981**, 29, 735
49. A. Vinogradov, S. Hashimoto. Mater *Trans* **2001**, 42, 74.
50. H. W. Hoppel, M. Kautz, C. Xu, M. Murashkin, T. G. Langdon, R. Z. Valiev, H. Mughrabi, *Int. J. Fatigue* **2006**, 28, 1001.
51. M. Murashkin, I. Sabirov, D. Prosvirnin, I. Ovidko, V. Terentiev, R. Valiev, S. Dobatkin. *Metals* **2015**, 5, 578.

Appendix I

The stress was estimated at all locations in the sample by using the basic bending equation (see **Equation 2)**. However, the geometry of the sample was not standard (see **Figure 11**). Hence to validate the estimation of the stress, finite element analysis was performed on the exact geometry of the sample using ANSYS. Firstly, the geometry of the sample was drawn in Solid Edge (see **Figure A1a**), which is then imported into ANSYS (see **Figure A1b**). Subsequently, boundary conditions appropriate to the fatigue loading are applied. Since the maximum stress for a test condition was known, the point force needed to generate the same maximum stress could be back-calculated using finite element analysis and subsequently stress at other locations in the gauge section was calculated. Once the stress contours were obtained (see **Figure A1c**)**,** the stress value along center path from the free end to the fixed end was calculated using standard post-processing tools of ANSYS. **Figure A2** shows the variation of the stress as function of distance away from the free-end (or the point where the load was applied), as obtained using FEA and **Equation** 2, and an excellent fit between these two methods was observed. This validates the use of **Equation 2** for calculating stress in the fatigue samples, even though its geometry was non-standard.

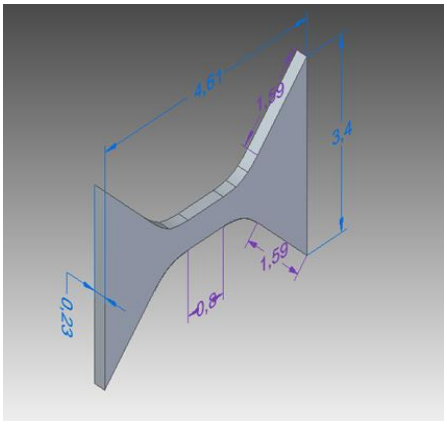

(a)

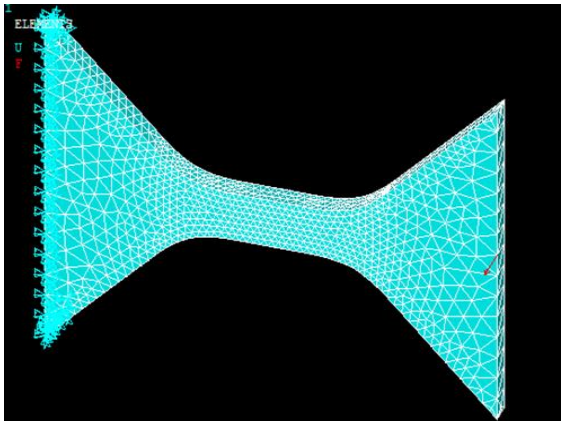

(b)

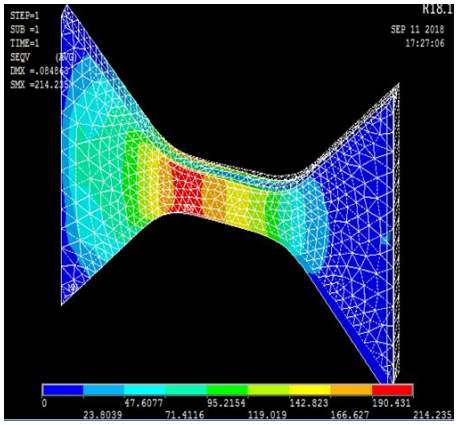

(c)

Figure A1: (a) The geometry of the fatigue sample used for FEA. All dimensions are in mm. (b) The discretized geometry along with the boundary condition applied to obtain the stress distribution in the sample. (c) The counter plot showing the normal stress distribution in the sample.

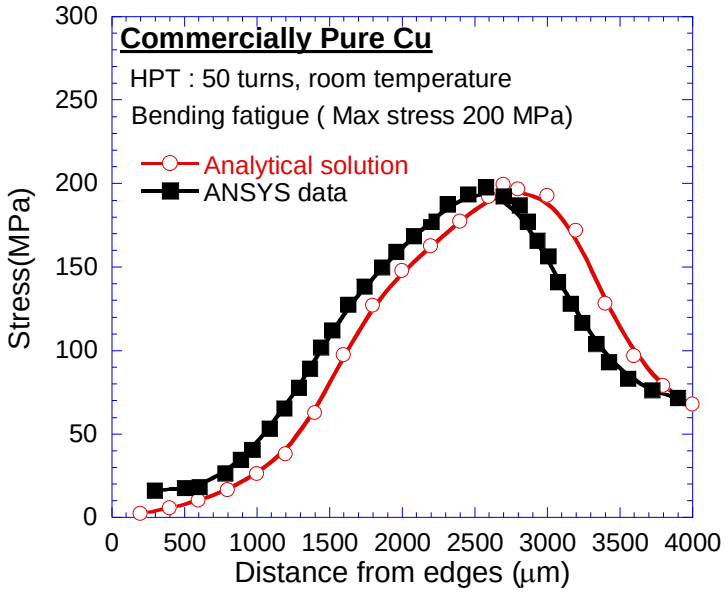

Figure A2: Comparison of the stress value calculated using **Eq. 2** and FEA performed using ANSYS.